creative commons
COMMONS DEED

저작자표시-비영리-변경금지 2.0 대한민국

이용자는 아래의 조건을 따르는 경우에 한하여 자유롭게

- 이 저작물을 복제, 배포, 전송, 전시, 공연 및 방송할 수 있습니다.

다음과 같은 조건을 따라야 합니다:

저작자표시. 귀하는 원저작자를 표시하여야 합니다.

비영리. 귀하는 이 저작물을 영리 목적으로 이용할 수 없습니다.

변경금지. 귀하는 이 저작물을 개작, 변형 또는 가공할 수 없습니다.

- 귀하는, 이 저작물의 재이용이나 배포의 경우, 이 저작물에 적용된 이용허락조건을 명확하게 나타내어야 합니다.
- 저작권자로부터 별도의 허가를 받으면 이러한 조건들은 적용되지 않습니다.

저작권법에 따른 이용자의 권리는 위의 내용에 의하여 영향을 받지 않습니다.

이것은 이용허락규약(Legal Code)을 이해하기 쉽게 요약한 것입니다.

Disclaimer

dCollection

ULSAN NATIONAL INSTITUTE OF
SCIENCE AND TECHNOLOGY

Master's Thesis

Synthesis of Cobalt-based Catalysts using Polyoxometalate for Electrochemical and Photoelectrochemical Water Oxidation

Yujin Han

Department of Energy Engineering

(Energy Engineering)

Graduate School of UNIST

2018

ULSAN NATIONAL INSTITUTE OF
SCIENCE AND TECHNOLOGY

Synthesis of Cobalt-based Catalysts using Polyoxometalate for Electrochemical and Photoelectrochemical Water Oxidation

Yujin Han

Department of Energy Engineering
(Energy Engineering)

Graduate School of UNIST

ULSAN NATIONAL INSTITUTE OF
SCIENCE AND TECHNOLOGY

Synthesis of Cobalt-based Catalysts using Polyoxometalate for Electrochemical and Photoelectrochemical Water Oxidation

A thesis
submitted to the Graduate School of UNIST
in partial fulfillment of the
requirements for the degree of
Master of Science

Yujin Han

06/ 07/ 2018

Approved by

_____

Advisor
Jungki Ryu

ULSAN NATIONAL INSTITUTE OF SCIENCE AND TECHNOLOGY

Synthesis of Cobalt-based Catalysts using Polyoxometalate for Electrochemical and Photoelectrochemical Water Oxidation

Yujin Han

This certifies that the thesis of Yujin Han is approved.

06/ 07 / 2018

signature

_____

Advisor: Jungki Ryu

signature

_____

Hyun-Kon Song

signature

_____

Hyun-Wook Lee

ULSAN NATIONAL INSTITUTE OF
SCIENCE AND TECHNOLOGY

Abstract

Highly efficient water-oxidation catalysts (WOCs) were readily prepared through the simple heat treatment of cobalt-containing polyoxometalate $[Co_4(H_2O)_2(PW_9O_{34})_2]^{10-}$ (POM). The annealing of soluble POM molecules at high temperatures in air led to the formation of insoluble nanoparticles, of which the crystal structure and catalytic activity can be controlled by the annealing temperature. POMs were converted to amorphous and crystalline $CoWO_4$ nanoparticles when annealed at 400 and 500 °C, respectively. Interestingly, amorphous $CoWO_4$ nanoparticles exhibited excellent catalytic activity near the neutral pHs, making them superior to both pristine POM and POM-derived crystalline $CoWO_4$ nanoparticles. Their outstanding performance was attributed to the optimum distance between the nearest Co ions, which facilitates the Langmuir-Hinshelwood (LH) mechanism that provides faster pathway of water oxidation than Eley-Rideal (ER) mechanism.

For its versatile application, however, its integration with a heterogeneous electrode/photoelectrode is critically required. Based on the findings on the synthesis of POM-derived WOCs by annealing, we could readily immobilize $CoWO_4$-based WOCs on the surfaces of various electrodes for efficient electrochemical and photoelectrochemical water oxidation through the annealing of POMs pre-adsorbed onto the desired electrode surface, such as porous carbon-felt electrodes and worm-like hematite photoanodes. In particular, we found that the photoelectrochemical performance of the hematite photoanode was significantly improved after the decoration with a-$CoWO_4$ WOCs in terms of photocurrent density and onset potential owing to the fast charge transfer and advantageous reaction pathway. This study may provide insights not only for the synthesis of efficient electrocatalysts derived from POMs but also for their immobilization onto the desired electrode surface for practical applications.

ULSAN NATIONAL INSTITUTE OF
SCIENCE AND TECHNOLOGY

ULSAN NATIONAL INSTITUTE OF SCIENCE AND TECHNOLOGY

Contents

ULSAN NATIONAL INSTITUTE OF SCIENCE AND TECHNOLOGY

ULSAN NATIONAL INSTITUTE OF
SCIENCE AND TECHNOLOGY

List of Figures

ULSAN NATIONAL INSTITUTE OF SCIENCE AND TECHNOLOGY

Figure 9. a) Ball and stick structure of Ru-substituted polyoxometalate having water oxidation capability, which have molecular formula of $[Ru_4(\mu\text{-}O)_4(\mu\text{-}OH)_2(H_2O)_4(\gamma\text{-}SiW_{10}O_{36})_2]^{10-}$. Combined polyhedral and ball and stick structure of $[Co_4(H_2O)_2(PW_9O_{34})_2]^{10-}$. Purple-Co atoms; red-O/OH_2 (terminal); Orange tetrahedral-PO_4 and gray octahedral- WO_6.

Figure 101. Schematic images for immobilization of various POMs to fabricate heterogeneous electrode. a) CNT-POM nanocomposite by amide bond followed by annealing at 120 ˚C for 24 h, b) POM@MOF (Fe) inorganic material synthesized by solvethermal method at 140 ˚C and c) organic-inorganic hybrid electrode fabricated by spin coating followed by annealing process.

Figure 11. Synthesis of $CoWO_4$-based WOCs by annealing of POM. Graphical illustration showing the structure of POM and the formation of POM-derived WOCs.

Figure 12. Schematic diagram of the basic principles of water splitting by photoelectrochemical cell with hematite as a photoanode. There are two pathways for charge carriers to follow depending on the presence of catalyst. In case of *i)* bare hematite, holes trapped in surface state can be consumed to recombination causing low faradaic efficiency but *ii)* hematite with WOCs, generated holes are transferred to catalyst faster to prevent recombination, leading improved water oxidation.

Figure 13. Structural change of POMs by annealing. (a, b) Photographs showing changes in (a) the color and (b) solubility of POMs upon annealing at various temperatures.

Figure 14. Several properties changed after heat treatment were analyzed by (a) Diffuse reflectance spectra (DRS) of POMs annealed at various temperatures, (b) TGA and DSC analysis of the pristine POM and (c) X-ray photoelectron spectra of pristine POMs and POMs annealed at various temperatures.

Figure 15. (a, b) TEM images of $CoWO_4$-based nanoparticles formed via annealing at (a) 400 and (b) 500 ˚C. The insets reveal the respective electron diffraction pattern. (c) XRD patterns and (d) Raman spectra of the pristine POMs and POMs annealed at 400 (POM400) and 500 ˚C (POM500).

Figure 16. Temperature-dependent properties of $CoWO_4$ WOCs prepared using precipitation methods. (a) Diffuse reflectance spectra of the respective $CoWO_4$ WOCs. (b) TGA and DSC analysis of a-$CoWO_4$. (c) XRD patterns and (d) Raman spectra of the respective $CoWO_4$.

Figure 17. Electrocatalytic water oxidation by the pristine POMs and POMs annealed at different temperatures. (a) Cyclic voltammograms and (inset) Tafel plots for the evaluation of their catalytic

ULSAN NATIONAL INSTITUTE OF SCIENCE AND TECHNOLOGY

activity. CV plots of various WOCs for the performance evaluation. (b) Comparison between POMs annealed at various temperatures. (c) The comparison between the POM-derived WOCs and a-$CoWO_4$ prepared using the precipitation method.

Figure 18. (a) Experimental scheme for the fabrication of an efficient anode for water oxidation via the deposition of POM400 on a carbon felt (CF) electrode. (b, c) SEM images and (d) cyclic voltammogram of the carbon felt electrode (b) before and (c) after the deposition of POM400 WOCs. The insets show the respective higher-magnification SEM image.

Figure 19. Identification of activity of cobalt as active sites of water oxidation. Cyclic voltammogram of POM w/o Co, POM w/o Co annealed at 400 $^{\circ}$C (POM w/o Co 400) and POM w/o Co 500.

Figure 20. Electrocatalytic water oxidation by the amorphous POM400 and crystalline POM500 that have different distance between nearest Co ions. Two suggested pathways of oxygen evolution reaction according to the Co-Co distance to explain outstanding performance of POM400.

Figure 21. Photoelectrochemical water oxidation using a hematite (Fe_2O_3) photoanode modified with POM400 WOCs. (a) Experimental scheme for the fabrication of an efficient photoanode using hematite and POM400. (d, e) Cross-sectional TEM images of the hematite photoanodes (b) before and (c) after the deposition of POM400. Raw and false-colored images were shown together for comparison. The insets show the respective EDS spectra for elemental analysis.

Figure 22. Spectroscopic analysis showing the deposition of POM400 on the surface of hematite photoanodes. (a) Diffuse reflectance and (b) Raman spectra of the photoanodes were compared before and after the deposition of POM400.

Figure 23. The photoelectrochemical performance of the bare and the modified hematite photoanodes were compared using (a) linear sweep voltammetry, (b) chronoamperometry at 1.3V *versus* RHE and (c) in terms of photocurrent densities and onset potentials.

Figure 24. (a) Electrochemical impedance spectra of the bare and modified hematite photoanodes were shown. The inset shows the equivalent circuit model for fitting and the magnified impedance spectra for the modified hematite photoanode. (b) Transfer efficiency plots calculated from J_{photo}-V curves of bare hematite and hematite covered with POM400.

Figure 25. Polarization curves measured in the presence (dotted lines) and absence (solid lines) of 0.1M

ULSAN NATIONAL INSTITUTE OF
SCIENCE AND TECHNOLOGY

H_2O_2 for the calculation of the transfer efficiency shown in Figure 24 (b).

Figure 26. The amount of evolved gases from a PEC cell using a hematite photoanode before and after the modification with POM400 that shows the enhancement of overall PEC performance

ULSAN NATIONAL INSTITUTE OF
SCIENCE AND TECHNOLOGY

List of Tables

ULSAN NATIONAL INSTITUTE OF SCIENCE AND TECHNOLOGY

1 Introduction

1.1 Research Backgrounds

In recent years, our excessive dependence on fossil fuels has caused severe environmental problems such as emissions of pollutants and greenhouse gases. Consequently, the development of clean and sustainable technologies enabling the production and utilization of energy resources has become urgently needed for both the present and future generations. Numerous researchers have extensively studied to develop such technologies, while the nature has already devised a system for sustainable energy conversion utilizing infinite solar energy, photosynthesis. In natural photosynthesis, electrons liberated by absorbed sunlight at the chloroplast are used to reduce CO_2 to carbohydrates and remaining vacancies are filled with electrons from electrochemical water oxidation. (Eq. 1)

$$2H_2O + h\nu \rightarrow O_2 + 4H^+ + 4e^- \qquad \text{(Eq. 1)}$$

By mimicking natural photosynthesis, various chemical fuels and compounds can be produced in an environmentally friendly and carbon-neutral manner by utilizing electrons from electrochemical water oxidation using solar energy (i.e., artificial photosynthesis) or renewable energies (water electrolysis). This is because water can act as a cheap and abundant source of electrons without the emission of any pollutants and greenhouse gases. For example, various forms of chemical compounds, such as hydrogen, CO, formate, and methanol, are produced using energetic electrons from electrochemical[1-3] or photoelectrochemical[4-6] water oxidation. As a result, it is the key for its realization to develop technologies to extract electrons efficiently from water oxidation and transfer to coupled reduction reaction to store the energy into the chemical bond.[7-8]

ULSAN NATIONAL INSTITUTE OF SCIENCE AND TECHNOLOGY

1.2 Introduction to Water Oxidation

1.2.1 Water Electrolysis

Water molecules can be electrochemically decomposed into oxygen and hydrogen ($2H_2O \rightarrow O_2 + 2H_2$) by applying a proper potential difference between two electrodes; a cathode and an anode where hydrogen evolution reaction (HER: $2H^+ + 2e^- \rightarrow H_2$) and oxygen evolution reaction (OER: $2H_2O \rightarrow O_2 + 4H^+ + 4e^-$) take place, respectively. (Figure 1) These half reactions also can be balanced with base as $2H_2O + 2e^- \rightarrow H_2 + 2OH^-$ (HER) and $4OH^- \rightarrow 2H_2O + O_2 + 4e^-$ (OER). In terms of thermodynamics, the standard cell potential ($E^o_{cell} = E^o_{cathode} - E^o_{anode}$) for water electrolysis is unchanged as -1.23V which means theoretical minimum energy required to operate the overall cell, while each half-cell potential can be varied depending on the pH based on Nernst equation. (Eq. 2)

$$E = E^o - \frac{RT}{nF} \ln \frac{a_{Red}}{a_{Ox}} \qquad \text{(Eq. 2)}$$

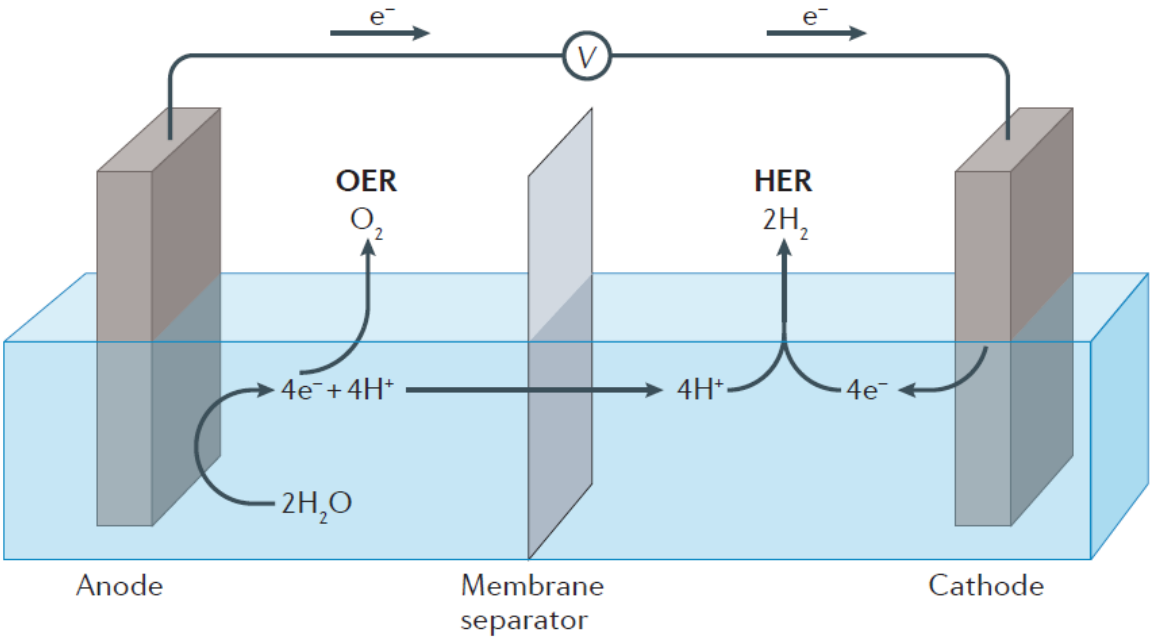

Figure 1. Schematic image showing overall water electrolysis including OER at anode and HER at cathode[9].

According to the Nernst equation, each half-cell potential (E) can be expressed in terms of the standard reduction potential (E^o) and activities of reduced and oxidized species (a). Chemical activities (a) are related to the concentration (c) via $a = rc$ where the r is an activity coefficient that can be approximated to unity under dilute conditions. As a result, each half-cell potentials can be simply

ULSAN NATIONAL INSTITUTE OF SCIENCE AND TECHNOLOGY

expressed using the pH of electrolysis solutions and several physical constants such as the gas constant (R, 8.314J $K^{-1}mol^{-1}$), temperature (T, 298K in case of reaction at room temperature), the number of electron transferred in the reaction (n=2 for HER and n=4 for OER), and the Faraday constant (F, 96485 C mol^{-1}), respectively. (Eq. 3 and Figure 2)

$$E_{HER} = -0.059pH, \qquad E_{OER} = 1.23V - 0.059pH \qquad \text{(Eq. 3)}$$

However, additional energy is required more than 1.23 V in practice due to overpotential for OER and HER. Of the two reactions, water oxidation reaction is a rate determining step due to its high activation energy and slow kinetics stemming from the complex reaction mechanism including many intermediates. (Figure 3)[10] As a result, OER requires a much higher overpotential than HER counterpart. Furthermore, it should be avoided that the active intermediates react to yield partially oxidized byproducts (e.g., HO·, H_2O_2)[11]. In this point of view, much efforts have been to devoted to develop efficient water oxidation catalysts (WOCs) by stabilizing these intermediates, leading faster and efficient water electrolysis.

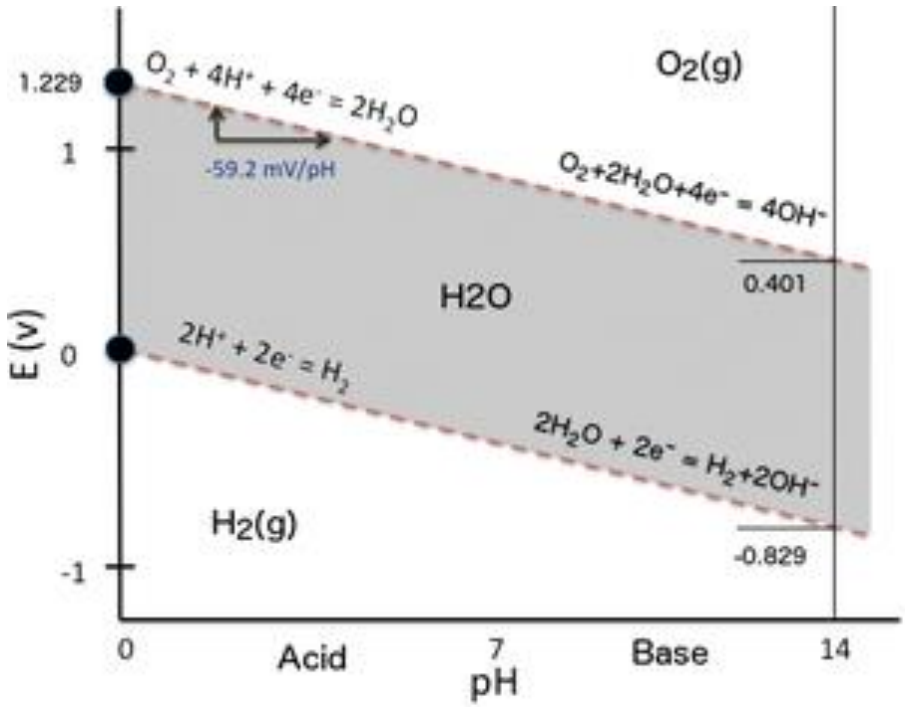

Figure 2. Pourbaix diagram showing each half cell potential required for oxygen and hydrogen evolution reactions as a function of the pH

ULSAN NATIONAL INSTITUTE OF
SCIENCE AND TECHNOLOGY

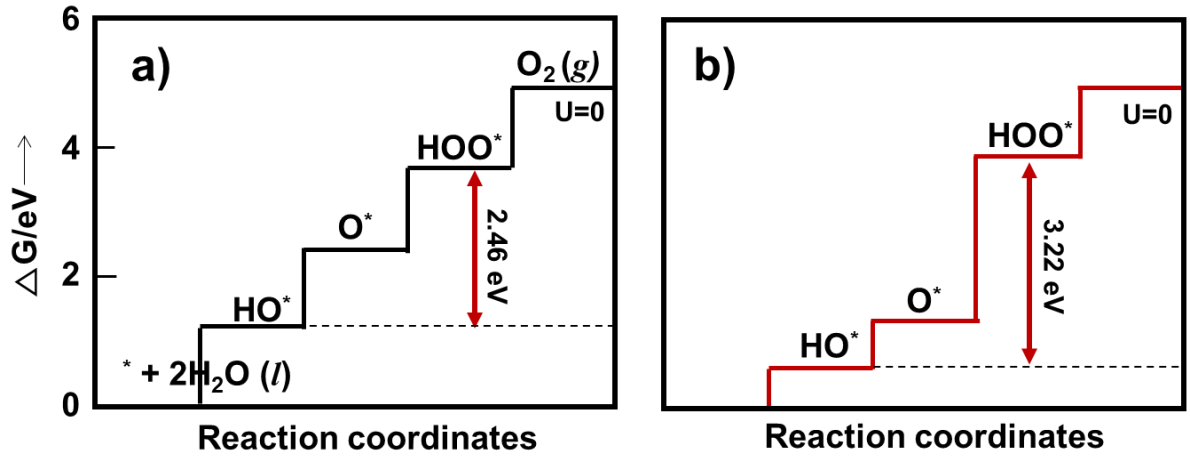

Figure 3. Standard free energies at U = 0 V for an (a) ideal catalyst and for (b) real catalyst (in here, $LaMnO_3$). For real catalysts, value for $\Delta G^0_{HOO*} - \Delta G^0_{HO*}$ (vertical line) has large barrier of 3.22 eV, whereas the ideal catalyst shows 2.46 eV. [10]

1.2.2 Artificial Photosynthesis

Natural photosynthesis is an energy harvesting process that all plants, algae, or microorganisms utilize for conversion of light energy into chemical products for their survival. It consists of light harvesting chlorophyll, electron transport system and water as a substrate. Based on the principles of light reactions, researchers have mimicked those components and incorporated into a working system that can produced chemical fuels using solar energy. (Figure 4)

ULSAN NATIONAL INSTITUTE OF SCIENCE AND TECHNOLOGY

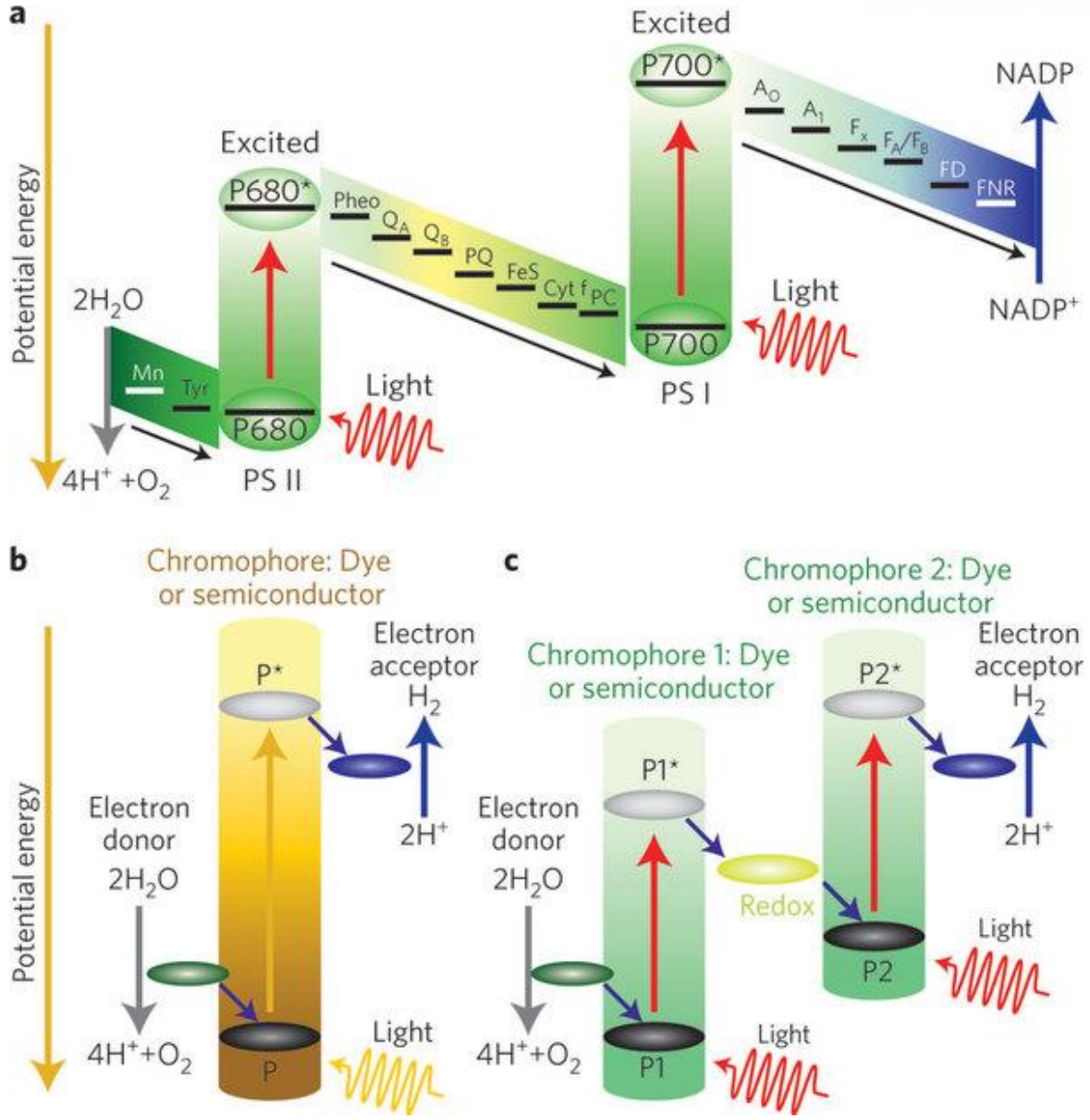

Figure 2. Schematic images of a) natural and b, c) artificial photosynthesis system with b) single step and c) two step reactions (Z-scheme) under light irradiation. Both systems take water as electron source which becomes oxygen at the catalyst.[12]

Compared to the combination of solar panels to a water electrolyzer (PV-electrolyzer), artificial photosynthesis (direct solar-to-fuel production) systems can directly convert solar energy to chemical energy, implying that the latter can have a higher theoretical efficiency as the more processes and connections between functional components are requires for the former. (Figure 5) Photoelectrochemical (PEC) cell, one of the device types of artificial photosynthesis, requires minimal components of two light absorbers (semiconductor photoelectrodes), electrocatalysts for redox reactions, a separator, and an electrolyte. Photoelectrodes are usually divided into two types;

ULSAN NATIONAL INSTITUTE OF SCIENCE AND TECHNOLOGY

photoanode where the oxidation reactions occur and photocathode where the reduction reactions do.

The basic principle of water splitting by PEC cells is described in Figure 6. It initiates its operation by generating free electrons via photoexcitation from the valence band (VB, E_v) to the conduction band (CB, E_c) of photoanodes by absorption of solar energy larger than its band-gap. Excited electrons flow towards counter electrode to reduce the substrate (e.g., H^+). It decides the products acquired from PEC cell which substrates are reduced at cathode interface. The vacancies, holes, remained after electron excitation are filled with electrons from water oxidation with a release of oxygen gas. Despite its huge potential for the production of chemical fuels in eco-friendly manner, artificial photosynthesis is suffered from low kinetics of water oxidation, resulting in a high overpotential. Hence, semiconductor photoelectrode with a bandgap much larger than 1.23 eV and light with a wavelength much shorter than the theoretically determined one (approximately 1000nm) are required for solar water splitting (Eq. 4). The relationship between wavelength of light and its photon energy is given by

$$E = h\nu \qquad \text{(Eq. 4)}$$

where, E is amount of energy [eV], ν is frequency [nm] and h is $6.6262X10^{-34}$ J·s, called Planck's constant.

Hence, various aspect of studies has been performed to lower the energy input in respect to structure or surface chemical composition of semiconductor[13], introduction of efficient water oxidation catalysts (WOCs), proper integrating method of catalyst onto the electrode, electrode with improved intrinsic properties and so on.

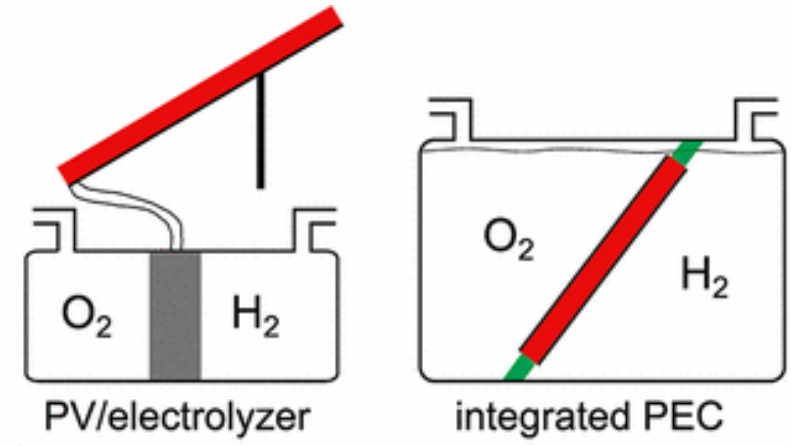

Figure 5. Two representative devices that convert solar power to chemical fuel, hydrogen. Left) Conventional combination of solar panel supplying electricity to discrete electrolyzer for water electrolysis. Right) Integrated photoelectrochemical cell where excited electrons are consumed directly by scavenger.[14]

ULSAN NATIONAL INSTITUTE OF
SCIENCE AND TECHNOLOGY

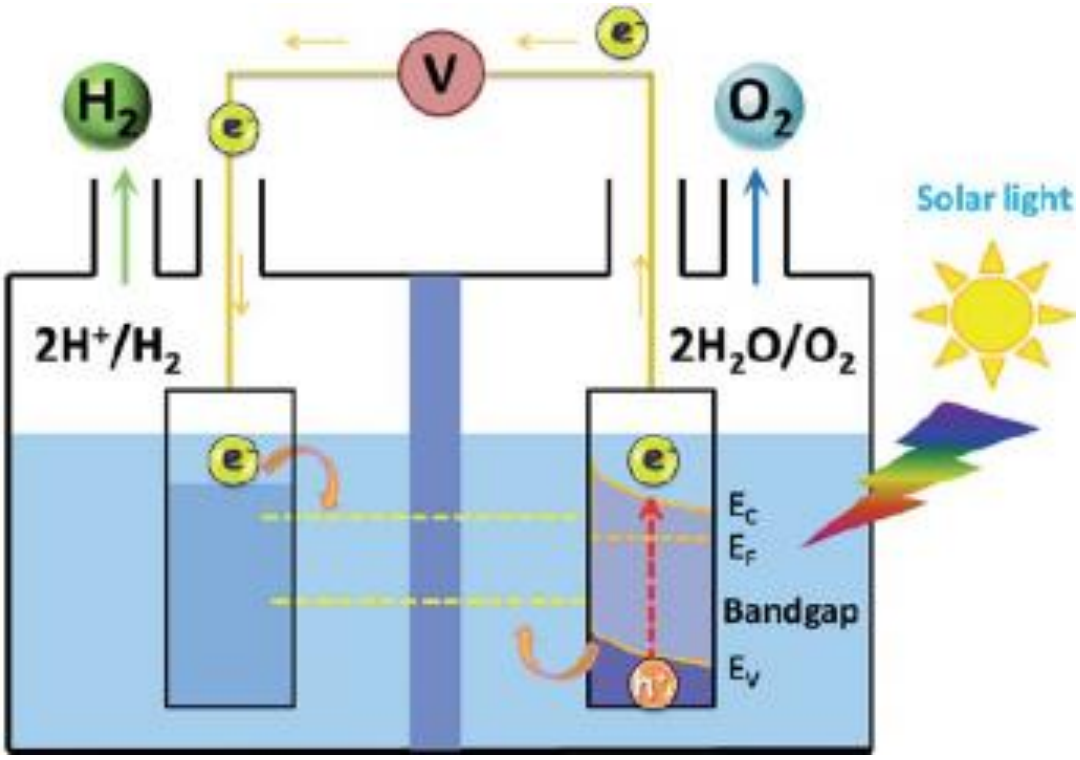

Figure 6. Schematic image of photoelectrochemical cell with connected wire that enables to produce products from anode and cathode separately. This system prevents the danger in the formation of explosive H_2 and O_2 mixture and problem about purity of fuel.[15]

1.3 Water Oxidation Catalysts (WOCs)

Among various strategies to address sluggish kinetics of water oxidation, in recent years, there has been a vigorous activity targeting the development of efficient water oxidation catalysts. It is highly demanded for both electrolysis of water with and without aid of light owing to its critical features that 1) facilitates the binding of water molecules to active sites which helps to by-pass the radical intermediates O· and HOO· and 2) leads immediate proximity for facile O-O collision and bond formation in the peroxo intermediate.(Figure 7)[16] Therefore, it lowers free energy of the highest energy intermediates of water oxidation and increase the efficiency of evolved oxygen by decreasing overpotential.

ULSAN NATIONAL INSTITUTE OF SCIENCE AND TECHNOLOGY

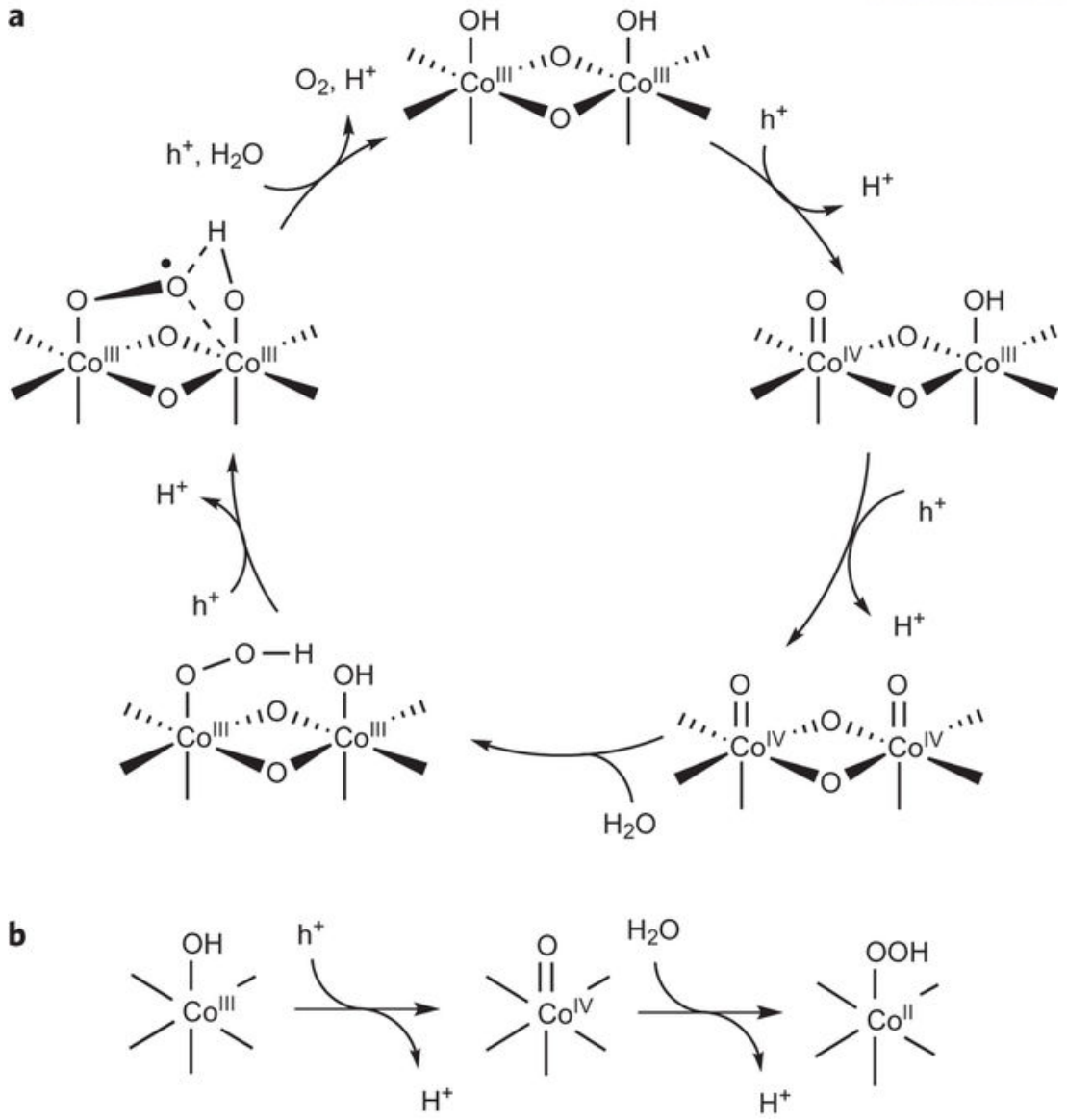

Figure 7. a) A fast mechanism and b) slow mechanism for water oxidation on Co_3O_4 surface site. The step forming O-O bond with H_2O in the fast mechanism features the aid of adjacent electronically coupled Co(IV) = O sites, which is not shown in the water oxidation at the slow mechanism. [17]

1.3.1 History and Limitations of Conventional WOCs

To overcome the complex mechanism of water oxidation for efficient oxygen evolution, numerous studies have been done on the synthesis of novel WOCs, such as organometallic compounds containing noble metals, including Ru[18] and Ir[19], transition metal oxide and perovskite nanomaterials,[20-22] and layered double hydroxides[23]. However, their intrinsic problems, such as the high cost and low stability of molecular homogeneous WOCs due to orgarnic lignads and low catalytic activity of

ULSAN NATIONAL INSTITUTE OF SCIENCE AND TECHNOLOGY

inorganic heterogeneous WOCs, have become a significant hurdle for their applications.[16, 24-25] (Figure 8)

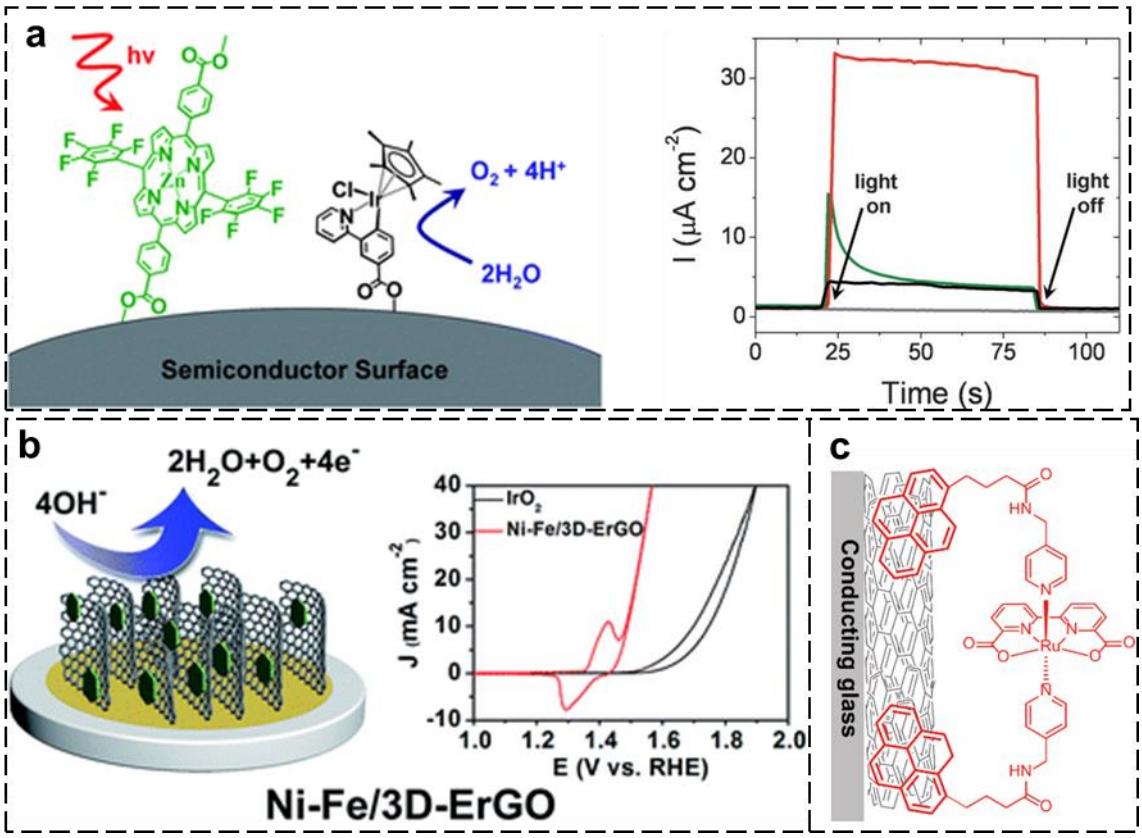

Figure 8. Various kinds of oxygen evolution catalyst reported to date. a) Ir-based WOCs including porphyrin [19], b) Ni–Fe layered double hydroxide/graphene electrode[23] and c) Ru WOCs assembled on multi-walled carbon nanotubes by π–π stacking. [18]

1.4 Polyoxometalates (POMs)

Polyoxometalates (POMs) are usually anions and consist of transition metal oxyanions (with chemical formula of $A_xO_y^{z-}$) connected by oxygen atoms forming discrete molecular structure, which can be regarded an intermediate of monometallic oxometallate and bulk metal oxide. POMs have been studied intensively as a promising WOCs because of its fast and reversible electron transfer reaction coming from their distinguished characteristics.[26] It has advantages resulting from reversible redox chemistries with transition metal at cores[27-28], high solubility in water, high stability with fully inorganic structure and tremendous number of exposed active sites with nanosized geometry. The possibility of POMs as a WOC was firstly reported by M. Bonchio[29] with Dawson-derived structure embedding a tetraruthenium-oxo-core. (Figure 9a) Another POM having four cobalt atoms, which are more economic than ruthenium, with molecular formula of $[Co_4(H_2O)_2(PW_9O_{34})_2]^{10-}$ was also reported by C. Hill.[30-31]

ULSAN NATIONAL INSTITUTE OF
SCIENCE AND TECHNOLOGY

Its structure was inspired by the oxo-bridged tetra-Mn complex of the oxygen evolution center in natural photosystem (PS) II, whose four manganese ions are corresponding to four cobalt ions placed in the center of Co_4POM. (Figure 9b)

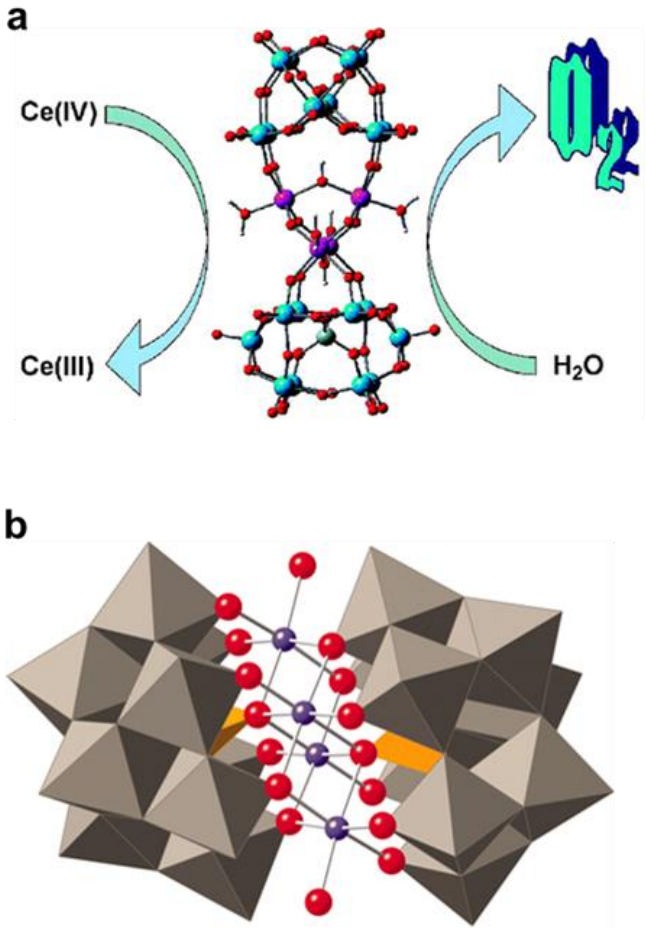

Figure 9. a) Ball and stick structure of Ru-substituted polyoxometalate having water oxidation capability, which have molecular formula of $[Ru_4(\mu\text{-}O)_4(\mu\text{-}OH)_2(H_2O)_4(\gamma\text{-}SiW_{10}O_{36})_2]^{10-}$. Combined polyhedral and ball and stick structure of $[Co_4(H_2O)_2(PW_9O_{34})_2]^{10-}$. Purple-Co atoms; red-$O/OH_2$ (terminal); Orange tetrahedral-PO_4 and gray octahedral- WO_6.

1.5 Research Objectives

As discussed in section 1.3 and 1.4, numerous studies have focused on improving catalytic activities and stability of WOCs, however, it is also essential to develop a simple method for immobilizing homogeneous catalysts onto the desired electrode surface or anchoring in the structure

ULSAN NATIONAL INSTITUTE OF SCIENCE AND TECHNOLOGY

for practical applications.[32-33] In this regard, there have been several approaches to anchoring POMs for heterogeneous structure. (Figure 10)

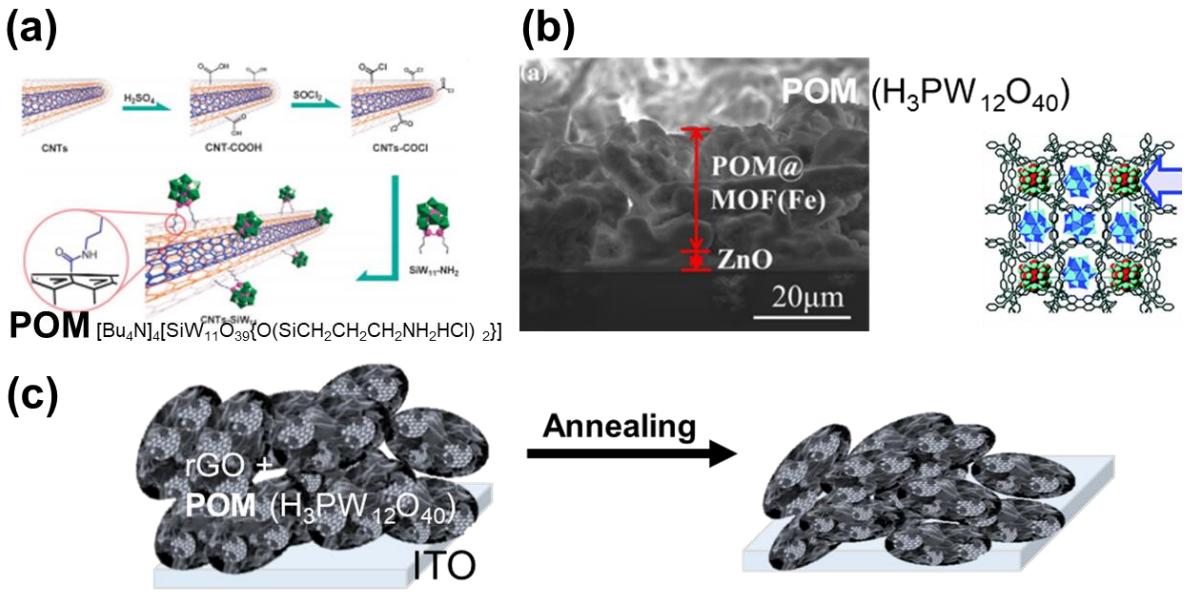

Figure 10. Schematic images for immobilization of various POMs to fabricate heterogeneous electrode. a) CNT-POM nanocomposite by amide bond followed by annealing at 120 ˚C for 24 h, b) POM@MOF (Fe) inorganic material synthesized by solvo-thermal method at 140 ˚C and c) organic-inorganic hybrid electrode fabricated by spin coating followed by annealing process.

Each research described in Figure 10 showed various immobilization strategies of POM by formation of amide bond[34], solvo-thermal method[35] and spin coating[36], including annealing process of POM. However, there is no further studies towards change of properties of POM resulting from heat treatment. Inspired by this niche, we designed the experiments to study thermal properties of POM and simple integrating strategy for heterogeneous configuration.

As a result, this research mainly focuses on 1) the investigation resulting from heat treatment to POM and 2) integrating highly efficient and stable electrode through the physical adsorption of POM molecules onto the desired surface following by annealing in air.

ULSAN NATIONAL INSTITUTE OF SCIENCE AND TECHNOLOGY

2 Experimental Section

2.1. Materials

$FeCl_3 \cdot 6H_2O$, $Co(NO_3)_2 \cdot 6H_2O$, $Na_2WO_4 \cdot 2H_2O$, and fluorine-doped tin oxide (FTO) glass (surface resistivity of 7 Ω/sq.) were purchased from Sigma-Aldrich (Saint Louis, MO, USA). $NaNO_3$ was purchased from Alpha Aesar (Hebrille, MA, USA). Na_2HPO_4 was obtained from Life Technologies. Carbon felt (through-plane resistivity < 12 Ω mm, in plane resistance < 4 Ω mm) was purchased from Fuelcell (Woburn, MA, USA).

2.2. Synthesis of POM and POM-Derived Water Oxidation Catalysts (WOCs)

$[Co_4(H_2O)_2(PW_9O_{34})_2]^{10-}$ was synthesized according to a previously reported method. Briefly, 1.08 M of $Na_2WO_4 \cdot 2H_2O$, 0.12M of Na_2HPO_4, and 0.24 M of $Co(NO_3)_2 \cdot 6H_2O$ were mixed in 50mL of water, followed by an adjustment of the pH to 7.0 with 1M HCl. The resultant precursor solution was refluxed at 100 °C for 2 h and was supersaturated with NaCl. Following the filtration of the saturated solution to remove NaCl and unreacted precursors, a pristine POM was obtained from recrystallization. The pristine POM was annealed at a desired temperature for 1 h with a ramping rate of 10 °C min^{-1} to synthesize POM-based WOCs.

2.3. Fabrication Method of Electrodes

2.3.1. Preparation of electrode modified with WOCs for electrochemical analysis

Working electrode for analysis of intrinsic electrochemical activity of WOCs is prepared on glassy carbon electrodes purchased from BASi (Cat. No. of MF-2012). After drying drop-casted solutions (5 μL of 1mM POM and POM-derived WOCs dissolved in 80mM phosphate buffer), drop-cast the 10 μL of Nafion® 117 solution (Sigma Aldrich, Cat. No. of 70160) whose pH is adjusted by NaOH to the neutral and dry. In case of $CoWO_4$, considering the concentration of cobalt ions which are thought to be active sites, 4mM amorphous $CoWO_4$ solution dissolved in 80mM phosphate buffer was analyzed instead of 1mM of that.

2.3.2. Preparation of Hematite Photoelectrodes

Hematite photoanodes were fabricated via a simple hydrothermal method followed by annealing. Briefly, a clean FTO substrate was placed in a 50mL Teflon-lined stainless steel autoclave containing an aqueous solution of 0.15M $FeCl_3$ and 0.1M $NaNO_3$ (10 mL) with the conductive side facing up. FeOOH nanorods were grown on the FTO substrate using a hydrothermal process at 100 °C for 1 h and then converted to a-Fe_2O_3 via annealing at 800 °C for 5 min. The processes were repeated twice.[32]

ULSAN NATIONAL INSTITUTE OF SCIENCE AND TECHNOLOGY

2.3.3. Deposition of WOCs onto surface

Negatively charged POMs were adsorbed onto the desired electrode surface, such as carbon felt and hematite, using a positively charged polyelectrolyte, such as branched poly(ethyleneimine), through electrostatic interactions. This adsorption process was repeated for a desired number of times to control the adsorbed amount of POMs. The electrode with the adsorbed POMs was annealed at 400 °C in air with a ramping rate of 10 °C min^{-1}.

2.4 Characterization

Morphology of samples was characterized using an S-4800 scanning electron microscope (SEM) (Hitachi High-Technologies, Japan) and a JEM-2100 transmission electron microscope (TEM) (JEOL, Japan) equipped with an energy dispersive X-ray spectrometer (EDS). Spectroscopic analyses were carried out using a Cary 5000 UV-Vis-NIR spectrophotometer (Agilent Technologies, Santa Clara, CA, USA), a D/MAX2500V/PC high-power X-ray diffractometer (XRD) (Rigaku, Japan), a q500 thermogravimetric analyzer (TGA) (TA instrument, USA), and an alpha 300R confocal Raman microscope (WITec, German).

2.5 Electrochemical and Photoelectrochemical Characterization

The performance of WOCs was evaluated using linear sweep voltammetry (LSV) and cyclic voltammetry (CV) using a WMPG1000 multichannel potentiostat/galvanostat and a 1260A electrochemical impedance spectroscopy (EIS) (Solartron, UK) in a three-electrode configuration: a working electrode, an electrode modified with WOCs; a counter electrode, Pt wire; and a reference electrode, Ag/AgCl filled with 1M KCl. For photoelectrochemical characterization, a 300W Xe lamp equipped with a 400nm cut-on filter (100 mW cm^{-2}) and a water infrared filter was used as a light source. All measurements were performed at least in triplicate for statistical analysis. Charge transfer efficiency was calculated by comparing LSV curves in an 80mM phosphate buffer with and without the addition of 0.1M H_2O_2 according to the following equation:[37-38]

$$\text{Transfer efficiency (\%)} = \frac{current\ density\ without\ H_2O_2}{current\ density\ with\ H_2O_2} \times 100$$

2.6 Gas Chromatography

A photoelectrochemical (PEC) cell (384mL) was filled with 50mL of an 80mM of phosphate buffer (pH of 8.0). The cell was sealed and purged with N_2 gas for 30 min before gas chromatography. A PEC cell was composed of a hematite working electrode, a Pt coil counter, and an Ag/AgCl reference electrode and was illuminated with a Xe lamp equipped with an ultraviolet and an infrared filter. For gas chromatography, a sample from the headspace of the PEC cell was collected using a gas-tight syringe and analyzed using a GC-2010 Plus gas chromatograph (Shimadzu Co., Japan).

ULSAN NATIONAL INSTITUTE OF SCIENCE AND TECHNOLOGY

3 Results and Discussion

3.1 Research Overview

Numerous researches dealing with catalytic activities of POMs have been studied after reported that they have efficient and robust performance for water oxidation by M. Bonchio.[29] There was, however, lack of researches towards thermal properties of POMs which is necessary to study since required annealing process for immobilization or fabrication of heterogeneous catalyst during electrode fabrication.[39-40] In this regards, POM with molecular formula of $[Co_4(H_2O)_2(PW_9O_{34})_2]^{10-}$ was annealed at various temperatures in air (POM annealed at 400 ˚C will be notated as POM400) to study their temperature-dependent structural and catalytic properties (Figure 11). In brief, POM after heat treatment was transformed to amorphous or crystalline $CoWO_4$-including WOCs with different catalytic activity.

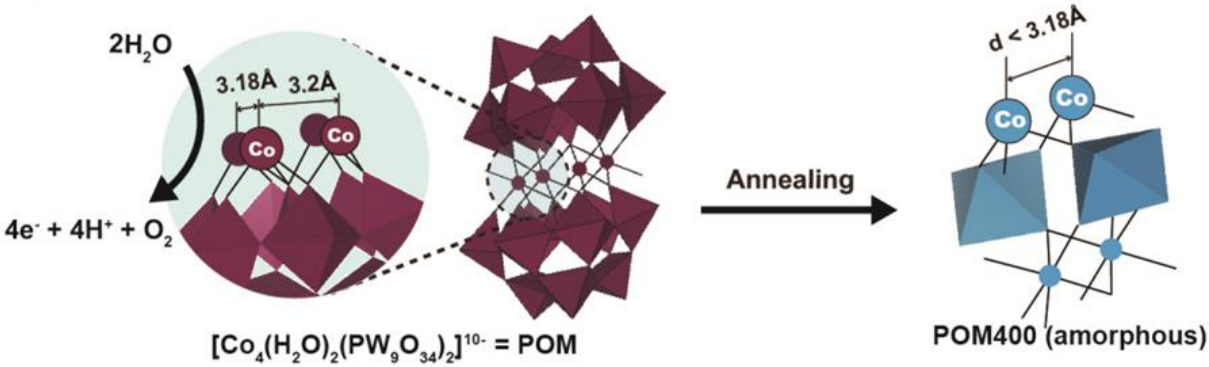

Figure 11. Synthesis of $CoWO_4$-based WOCs by annealing of POM. Graphical illustration showing the structure of POM and the formation of POM-derived WOCs.

Encouraged by these findings, finally, it was attempted to fabricate efficient water oxidation anode for photoelectrochemical cell by depositing POM onto photoelectrode followed by heat treatment at optimized temperature. Consequently, we showed that WOCs covering the interface of photoelectrode let the resistance of hole transfer lower, leading efficient hydrogen production. (Figure 12)

ULSAN NATIONAL INSTITUTE OF
SCIENCE AND TECHNOLOGY

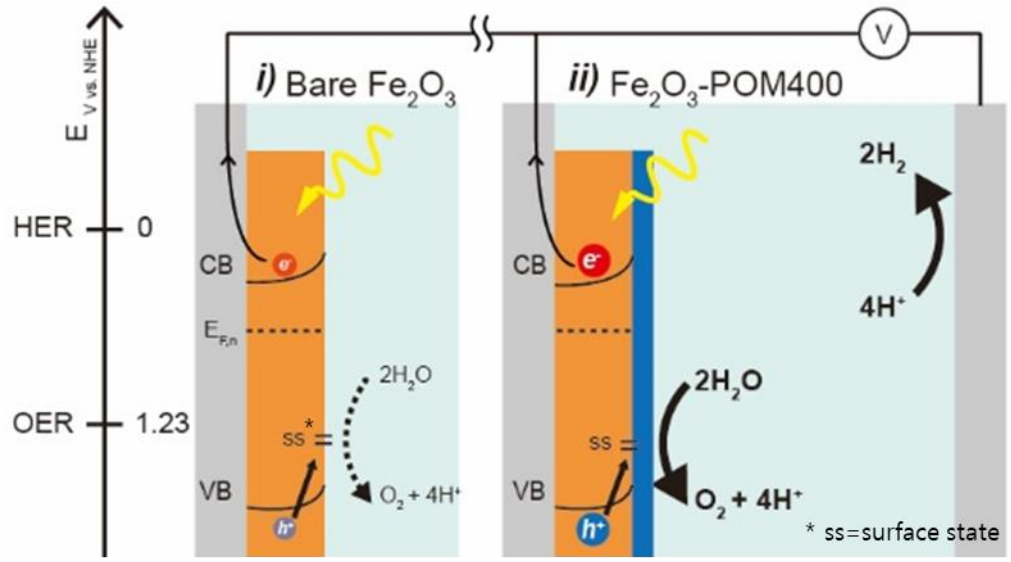

Figure 12. Schematic diagram of the basic principles of water splitting by photoelectrochemical cell with hematite as a photoanode. There are two pathways for charge carriers to follow depending on the presence of catalyst. In case of *i)* bare hematite, holes trapped in surface state can be consumed to recombination causing low faradaic efficiency but hematite with WOCs, generated holes are transferred to catalyst faster to prevent recombination, leading improved water oxidation.

ULSAN NATIONAL INSTITUTE OF SCIENCE AND TECHNOLOGY

3.2 Characterizations

Most notably, the annealing of POMs resulted in a color change: violet at 300 °C or below, cobalt blue at 400 °C (POM400), dark green at 500 °C (POM500), and light blue at 600 °C or above (Figure 13a). Accordingly, the solubility of POMs and POM-derived nanoparticles in water was dramatically changed also at 400 °C where the notable color change was first observed. Whereas pristine POMs and POMs annealed below 300 °C were highly soluble in water, POMs annealed at 400 °C and above became insoluble showing precipitation after placing it for a while. (Figure 13b).

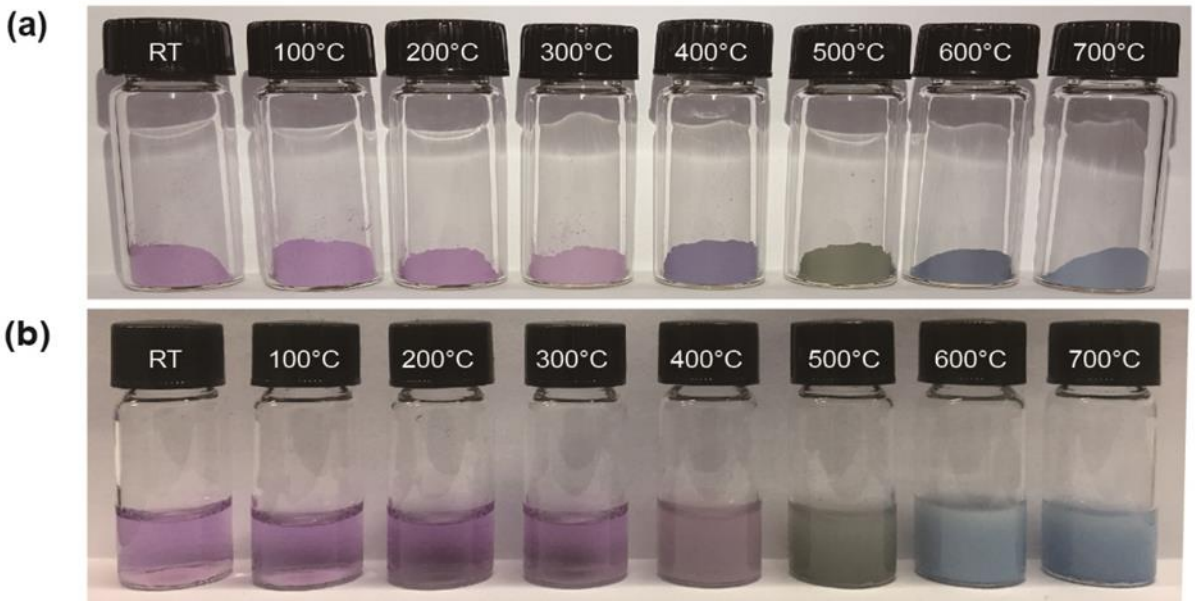

Figure 13. Structural change of POMs by annealing. (a, b) Photographs showing changes in (a) the color and (b) solubility of POMs upon annealing at various temperatures.

A distinct absorbance peak of pristine POMs at around 560 nm was red-shifted following the heat treatment. Thermogravimetric analysis (TGA), differential scanning calorimetry (DSC) showed rapid drop and endothermic peak around 100 °C respectively, owing to desorption of water from hydrate POM. Moreover, TGA and ex-situ X-ray photoelectron spectroscopy (XPS) revealed an endo- and an exo-thermic peak at around 250 and 450 °C with a negligible change in mass and elemental composition, implying the phase transitions of POMs (Figure 14)

ULSAN NATIONAL INSTITUTE OF SCIENCE AND TECHNOLOGY

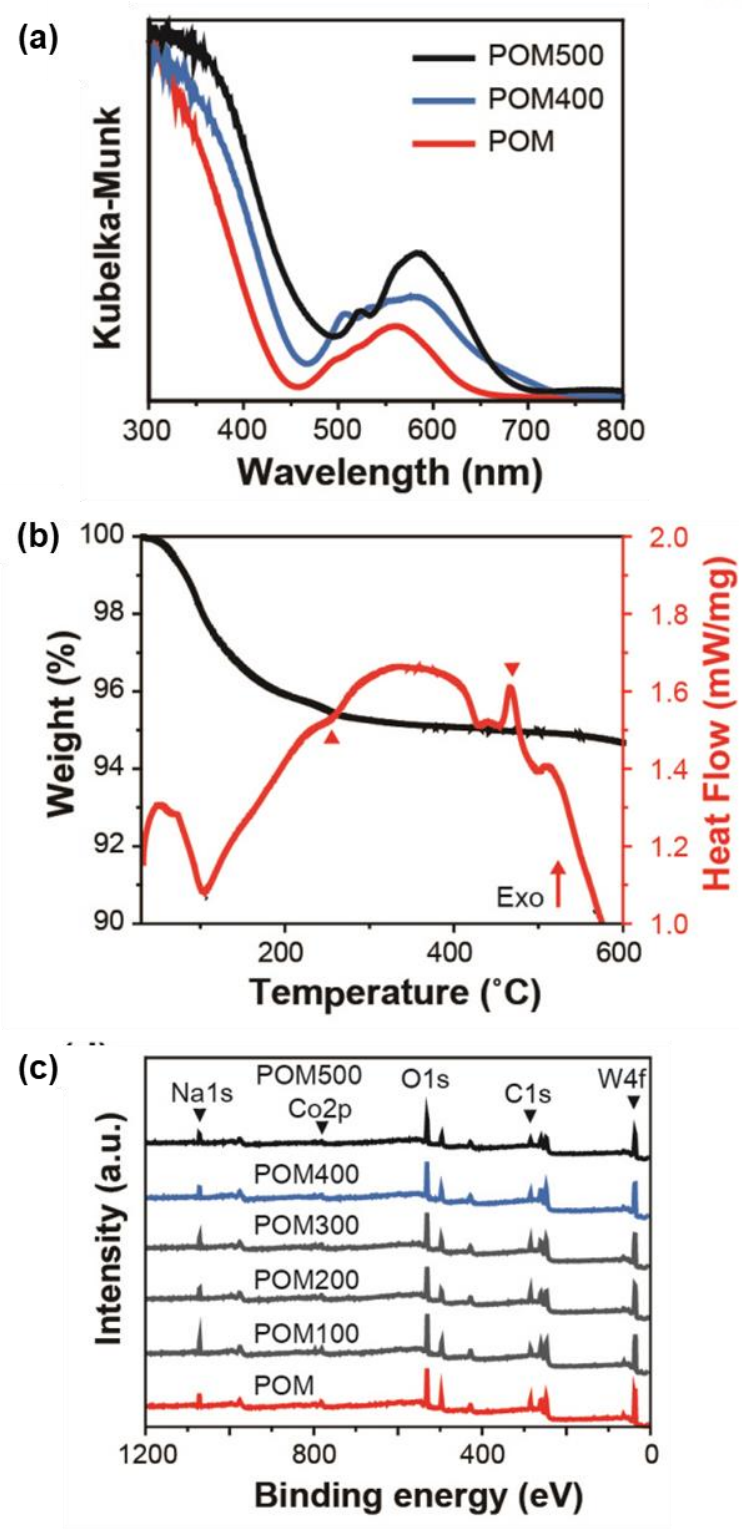

Figure 14. Several properties changed after heat treatment were analyzed by (a) Diffuse reflectance spectra (DRS) of POMs annealed at various temperatures, (b) TGA and DSC analysis of the pristine POM and (c) X-ray photoelectron spectra of the pristine POMs and POMs annealed at various temperatures.

ULSAN NATIONAL INSTITUTE OF
SCIENCE AND TECHNOLOGY

The morphology of Transmission electron microscopy (TEM) revealed that the annealing of POM with a diameter of less than 2 nm at high temperatures resulted in the formation of nanoparticles on a scale of several tens of nm (Figure 15a, b). Electron diffraction analysis revealed that the POM400 and POM500 were in the amorphous and crystalline phases, respectively (insets of Figure 15a, b). The result of the X-ray diffraction (XRD) analysis (Figure 15c) was consistent with that of TEM. Although no peaks were observed for the POM400, characteristic peaks of monoclinic $CoWO_4$ (ICDD 01-072-0479) and orthorhombic $Na_2W_2O_7$ (ICDD 01-073-0554) appeared for the POM500, indicating the formation of binary mixed crystalline materials. Interestingly, the characteristic Raman peaks corresponding to WO_4 for the amorphous POM400 were blue-shifted compared with those for the crystalline POM500 (Figure 15d). Considering that a blue shift is frequently observed when compressive stress exists,[35] it was thought that the POM400 with a-$CoWO_4$ had a more compact structure compared with the pristine POM and POM500 with c-$CoWO_4$. The formation of $CoWO_4$ from the POM can also be indirectly demonstrated by comparing the temperature-dependent properties of amorphous $CoWO_4$ (a-$CoWO_4$), which was prepared via the precipitation method,[36] with those of the POM400. a-$CoWO_4$ also underwent a phase transition to crystalline $CoWO_4$ (c-$CoWO_4$) with a similar color change upon annealing but at a lower temperature of 400 $^{\circ}$C (Figure 16). Similarly, a red shift of the Raman spectra was observed upon the formation of c-$CoWO_4$ from a-$CoWO_4$. These results clearly support the formation of a- and c- $CoWO_4$ nanoparticles from the POM via simple heat treatment.

ULSAN NATIONAL INSTITUTE OF
SCIENCE AND TECHNOLOGY

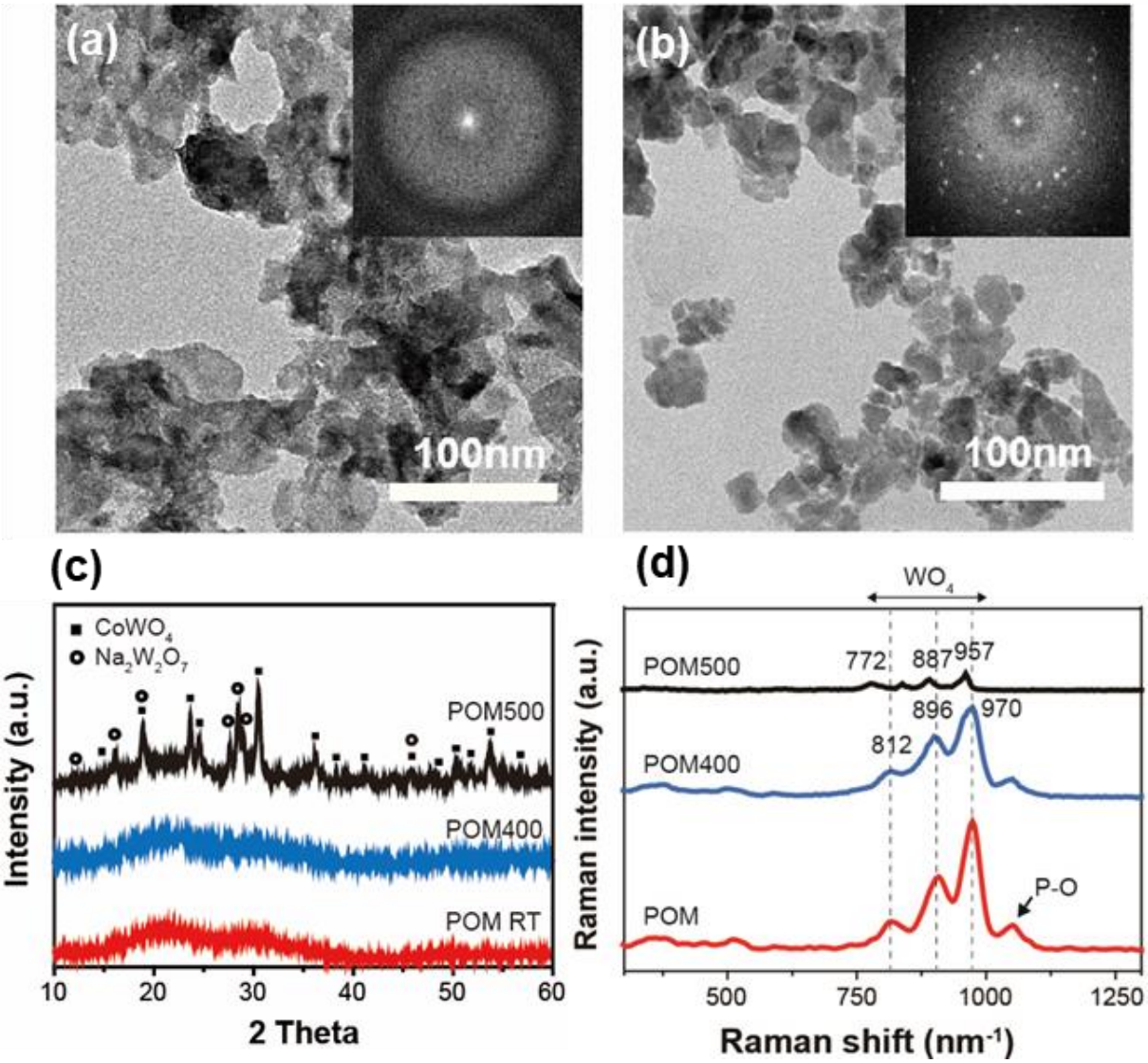

Figure 15. (a, b) TEM images of $CoWO_4$-based nanoparticles formed via annealing at (a) 400 and (b) 500 ˚C. The insets reveal the respective electron diffraction pattern. (c) XRD patterns and (d) Raman spectra of the pristine POMs and POMs annealed at 400 (POM400) and 500 ˚C (POM500).

ULSAN NATIONAL INSTITUTE OF
SCIENCE AND TECHNOLOGY

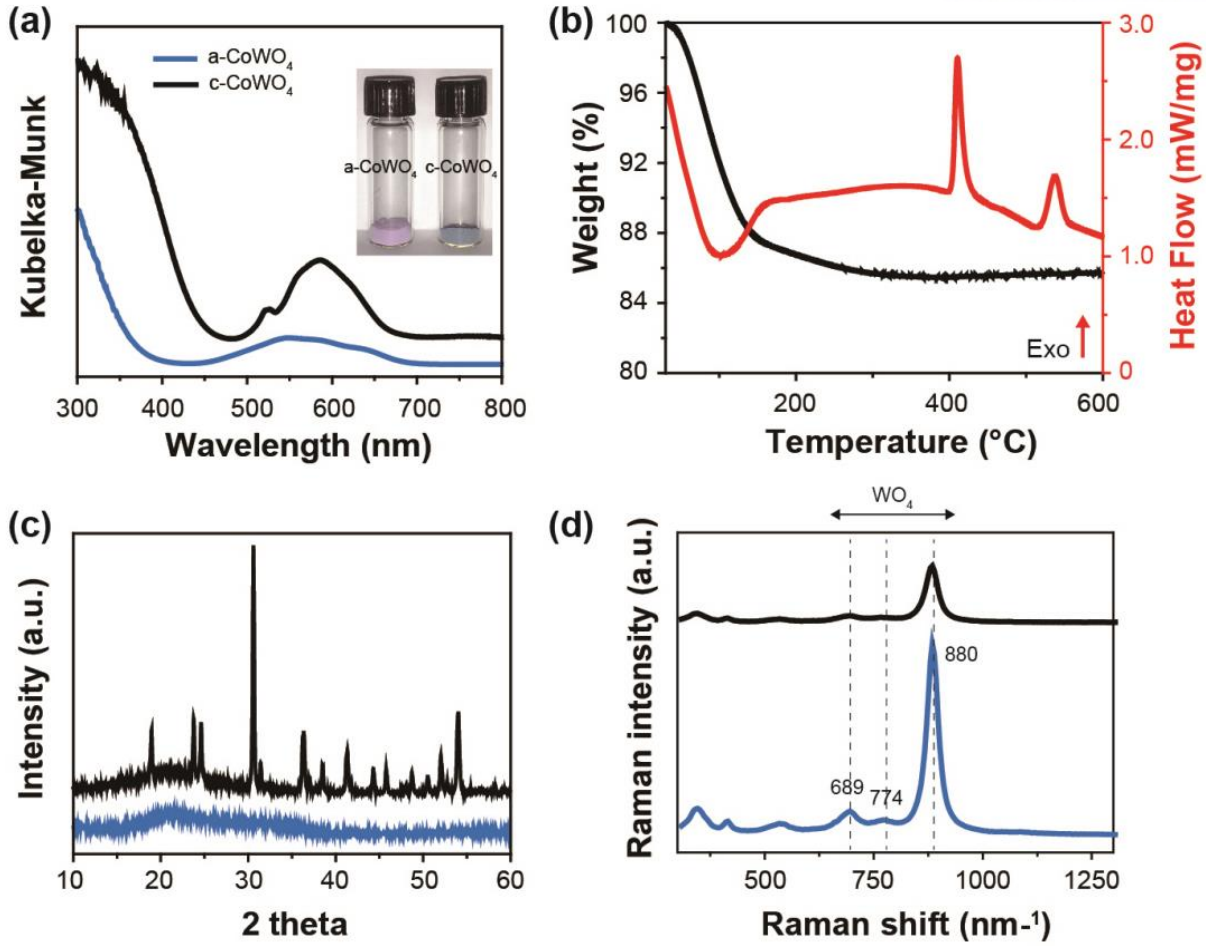

Figure 16. Temperature-dependent properties of $CoWO_4$ WOCs prepared using precipitation methods. (a) Diffuse reflectance spectra of the respective $CoWO_4$ WOCs. (b) TGA and DSC analysis of a-$CoWO_4$. (c) XRD patterns and (d) Raman spectra of the respective $CoWO_4$.

ULSAN NATIONAL INSTITUTE OF SCIENCE AND TECHNOLOGY

3.3 Electrochemical Catalytic Activity

3.3.1 Analysis of Electrochemical Catalytic Activity

Based on these findings, the catalytic activity of POMs and POM-derived nanoparticles for water oxidation was investigated using cyclic voltammetry (CV) at around neutral pHs (Figure 17a). Pristine POMs exhibited moderate performance with an onset potential of 1.63 V *versus* reversible hydrogen electrode (RHE) and a Tafel slope of 144 mV dec^{-1}. The annealing of POMs resulted in a dramatic change in their catalytic activity as well as in their crystal structure. POMs treated at 400 ˚C or below exhibited an improved catalytic activity, whereas POMs treated at 500 ˚C or above with c-$CoWO_4$ exhibited a degraded catalytic activity (Figure 17b). Among various POM-derived nanoparticles, POM400 with a-CoWO4 exhibited the best performance with an onset potential of 1.41 V *versus* RHE and a Tafel slope of 80 mV dec^{-1}. Overpotentials at a current density of 100mA cm^{-2} mol_{Co} for the POM, POM400, and POM500 were 0.498, 0.385, and 0.55 V, respectively. Interestingly, the POM400 exhibited a much higher catalytic activity compared with a-$CoWO_4$ prepared using the precipitation method and the pristine POM (Figure 17c), suggesting a new approach to the synthesis of WOCs. In addition to, we attempted to fabricate an efficient water oxidation anode by depositing the POM400 on a porous carbon-felt (CF) electrode. For the deposition of the POM400, pristine POMs with a high negative charge were adsorbed onto the CF electrode using a cationic polyelectrolyte through electrostatic interactions, and then, they were annealed at 400 ˚C for 1 h for the formation of a-$CoWO_4$ and the removal of the polyelectrolyte (Figure 18a). After such a simple treatment, the CF electrode was readily and uniformly coated with POM400 nanoparticles (Figure 18b, c) and exhibited outstanding performance for water oxidation even at a pH of 8.0. The overpotentials at current densities of 10 and 100 mA cm^{-2} were 0.392 and.0.72 V, respectively, which is highly impressive given that these measurements were carried out at around neutral pHs.(Figure 18d)

ULSAN NATIONAL INSTITUTE OF
SCIENCE AND TECHNOLOGY

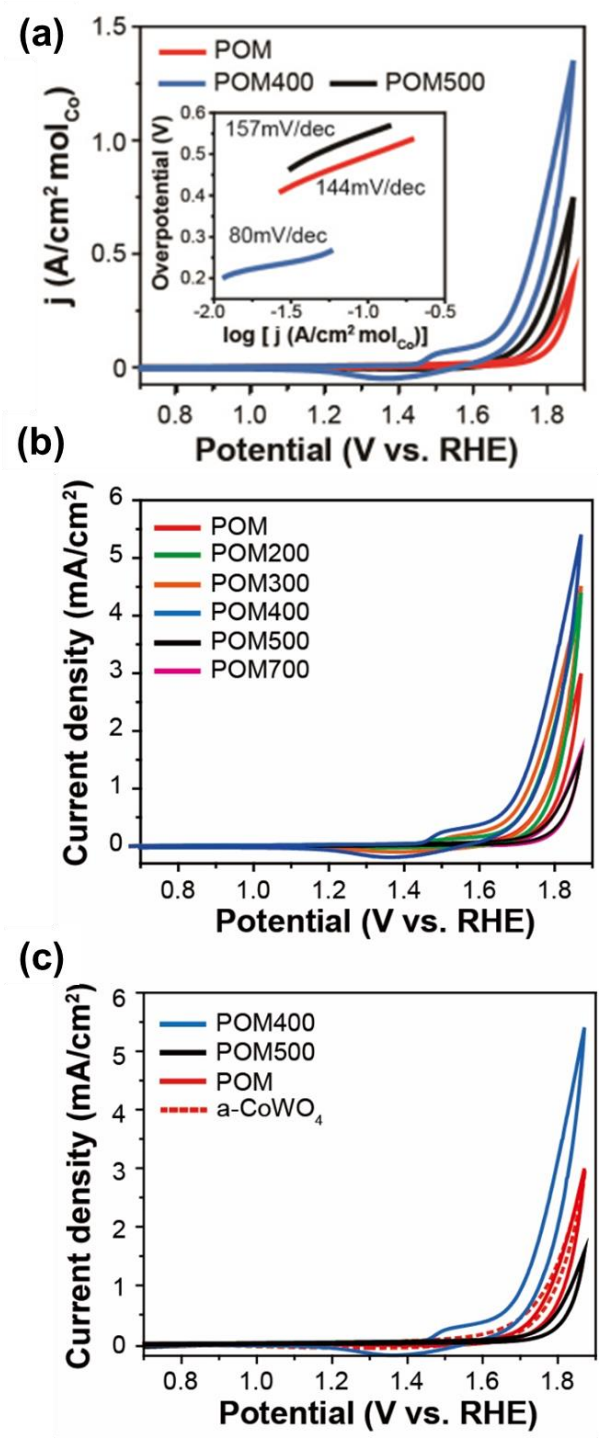

Figure 17. Electrocatalytic water oxidation by the pristine POMs and POMs annealed at different temperatures. (a) Cyclic voltammograms and (inset) Tafel plots for the evaluation of their catalytic activity. CV plots of various WOCs for the performance evaluation. (b) Comparison between POMs annealed at various temperatures. (c) Comparison between the POM-derived WOCs and a-$CoWO_4$ prepared using the precipitation method.

ULSAN NATIONAL INSTITUTE OF
SCIENCE AND TECHNOLOGY

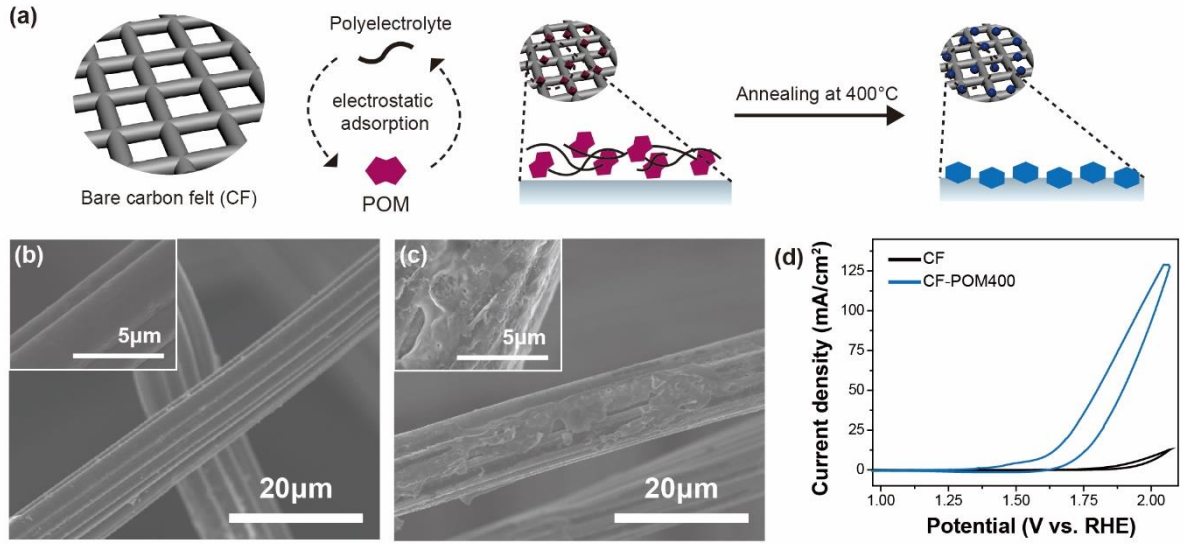

Figure 18. (a) Experimental scheme for the fabrication of an efficient anode for water oxidation via the deposition of POM400 on a carbon felt (CF) electrode. (b, c) SEM images and (d) cyclic voltammogram of the carbon felt electrode (b) before and (c) after the deposition of POM400 WOCs. The insets show the respective higher-magnification SEM image.

3.3.2 Proposed Principle for Enhanced Activity

The outstanding performance of the POM400 can be explained in terms of various water oxidation mechanisms dependent on the distance between the nearest neighboring Co^{2+} ions ($D_{Co2+-Co2+}$) which interact with water molecules as active sites. It was figured out via cyclic voltammetry of POM without Co ions (POM w/o Co) that showing negligible current compared to that of POM or WOCs originated from POM. (Figure 19) Moreover, electrochemical catalytic activities of POM w/o Co and its derivatives didn't display any increasement after heat treatment. We thought this supported the role of cobalt ions in water oxidation process.

ULSAN NATIONAL INSTITUTE OF SCIENCE AND TECHNOLOGY

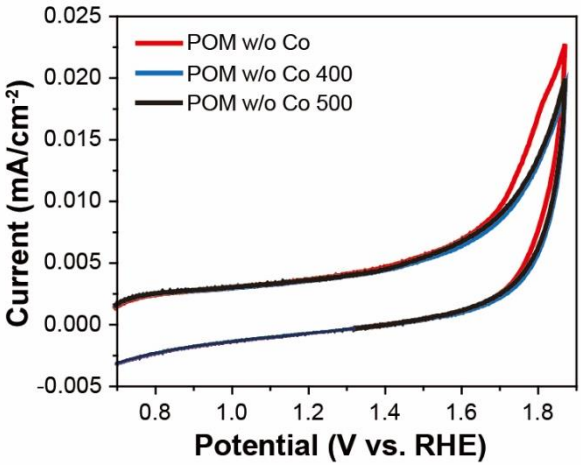

Figure 19. Identification of activity of cobalt as active sites of water oxidation. Cyclic voltammogram of POM w/o Co, POM w/o Co annealed at 400 ˚C (POM w/o Co 400) and POM w/o Co 500.

According to the literature, a red shift of characteristic Raman peaks suggests the presence of compressive stress[35] and the mechanism of electrocatalytic water oxidation highly depends on the distance between the active site (Co^{2+} ions in this study) for water oxidation (Figure 20).[41] When $D_{Co2+-Co2+}$ is comparable to the bond length of molecular oxygen, the water oxidation reaction may follow the Langmuir-Hinshelwood (LH) mechanism where molecular oxygen is formed by reactions between oxygen species adsorbed onto two neighboring active sites. In contrast, when $D_{Co2+-Co2+}$ is much larger than the bond length is, it may follow the Eley-Rideal (ER) mechanism, where molecular oxygen is formed from the single active site. According to the literature, $D_{Co2+-Co2+}$ is much shorter for a-$CoWO_4$ (2.82 Å) than for c-$CoWO_4$ (4.69 Å),[41] meaning that a- and c-$CoWO_4$ may follow the LH and ER mechanisms, respectively. The ER mechanism requires a higher overpotential compared with the LH mechanism because it requires thermodynamically less-favorable processes for the complete water oxidation.[41-42] In the same manner, the POM400 with a-$CoWO_4$ and the POM500 with c-$CoWO_4$ may follow the LH and ER mechanisms, respectively. Interestingly, the POM400 exhibited much higher catalytic performance than did pure a-$CoWO_4$ prepared using the precipitation method (Figure 17c). It is thought that the Co^{2+}-Co^{2+} distance varies even in a-$CoWO_4$ due to its disordered nature, meaning that only a small portion of Co^{2+}-Co^{2+} pairs follow the LH mechanism. In contrast, it is thought that a large portion of Co^{2+}-Co^{2+} pairs are present and follow the LH mechanism for a POM400 because raw material for a POM400 (i.e., a POM) has a cluster of Co^{2+} ions with a nearest neighbor distance of 3.18 Å.

ULSAN NATIONAL INSTITUTE OF
SCIENCE AND TECHNOLOGY

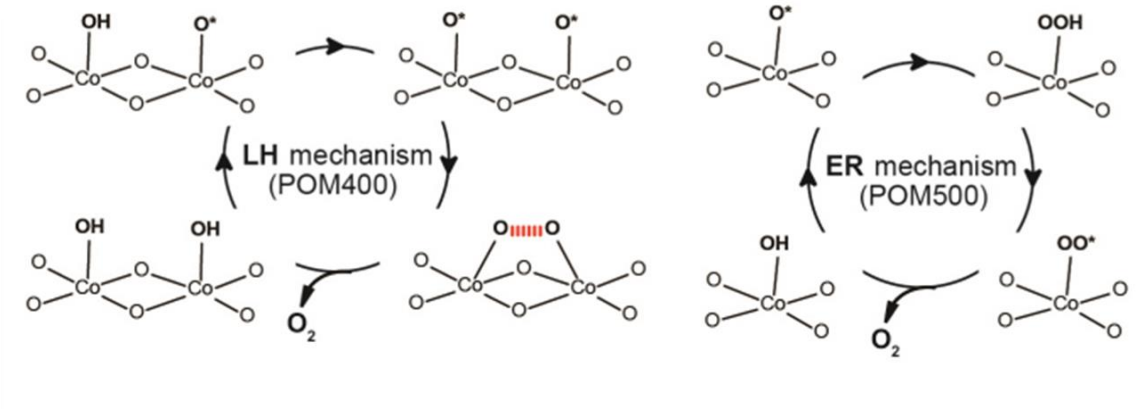

Figure 20. Electrocatalytic water oxidation by the amorphous POM400 and crystalline POM500 that have different distance between nearest Co ions. Two suggested pathways of oxygen evolution reaction according to the Co-Co distance to explain outstanding performance of POM400.

ULSAN NATIONAL INSTITUTE OF SCIENCE AND TECHNOLOGY

3.4 Analysis of Photoelectrochemical Catalytic Activity

3.4.1 Characterizations

Our approach was also tested to construct a water oxidation photoanode by decorating α-Fe_2O_3 (hematite) with POM400 as a cocatalyst. Hematite is regarded a promising photoanode due to its abundance, moderate band gap, and suitable band edge position for water oxidation [38-40]. Due to its sluggish water oxidation kinetics, however, it should be modified with WOCs. Here, the POM400 was readily deposited on the hematite photoanode via high temperature annealing following the pre-adsorption of the pristine POMs (Figure 21). Prominent difference of surface morphology was observed before and after deposition of POM400. Scanning electron microscope (SEM) images presented POM400 nanoparticles immobilized on warm-like hematite photoelectrode via electrostatic adsorption and annealing. (Figure 21b, c) Uniform and conformal coating of POM400 catalyst layer on the rough hematite photoanode is more clearly shown in cross-sectional TEM images where the area painted with blue or orange expressed POM400 and hematite respectively. (Figure 21d, e) It was observed that POM400 catalyst forms not only tangled nanoparticles, but catalyst layer with a few tens of nanometers uniformly. It was also proved by energy-dispersive X-ray spectroscopy (EDS). EDS spectrum of hematite on FTO electrode showed peaks corresponding to the iron and tin, but that of hematite electrode modified with POM400 displayed additional tungsten, phosphorus and cobalt signal. The signal of cobalt was presented on both bare and modified hematite since it was overlapped with the signal from nickel TEM grid which has similar energy level to the cobalt. Nevertheless, the intensity was increased twice from 0.97 to 1.98, indicating the deposition of POM400 on hematite photoelectrode. The formation of the POM400 layer on the hematite photoanode was also confirmed via the diffuse reflectance and Raman spectra (Figure 22). It is noteworthy here that the formation of the POM400 layer had a negligible effect on the absorbance of the underlying photoanode due to a relatively small amount of the POM400.

ULSAN NATIONAL INSTITUTE OF SCIENCE AND TECHNOLOGY

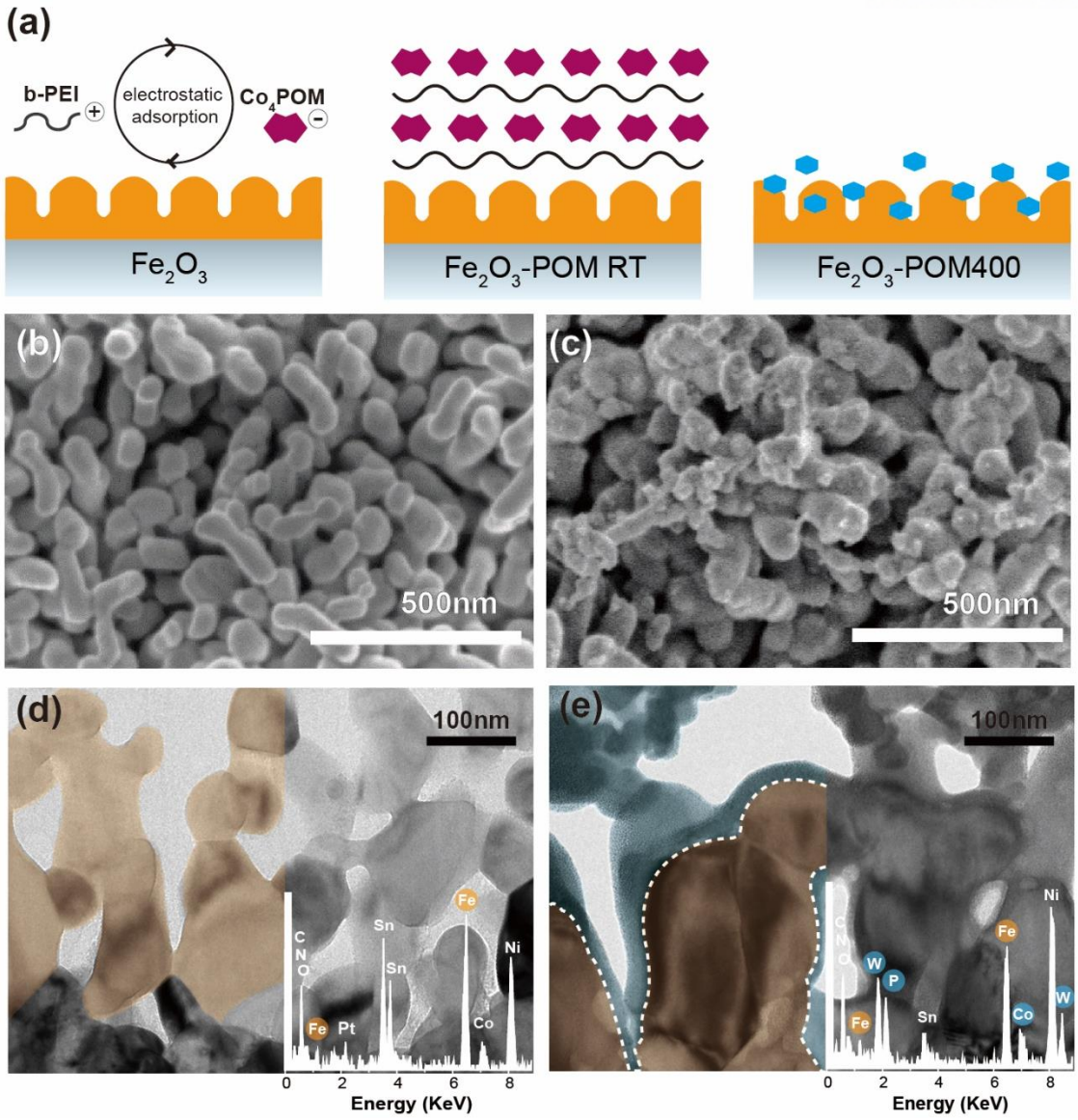

Figure 21. Photoelectrochemical water oxidation using a hematite (Fe_2O_3) photoanode modified with POM400 WOCs. (a) Experimental scheme for the fabrication of an efficient photoanode using hematite and POM400. (d, e) Cross-sectional TEM images of the hematite photoanodes (b) before and (c) after the deposition of POM400. Raw and false-colored images were shown together for comparison. The insets show the respective EDS spectra for elemental analysis.

ULSAN NATIONAL INSTITUTE OF
SCIENCE AND TECHNOLOGY

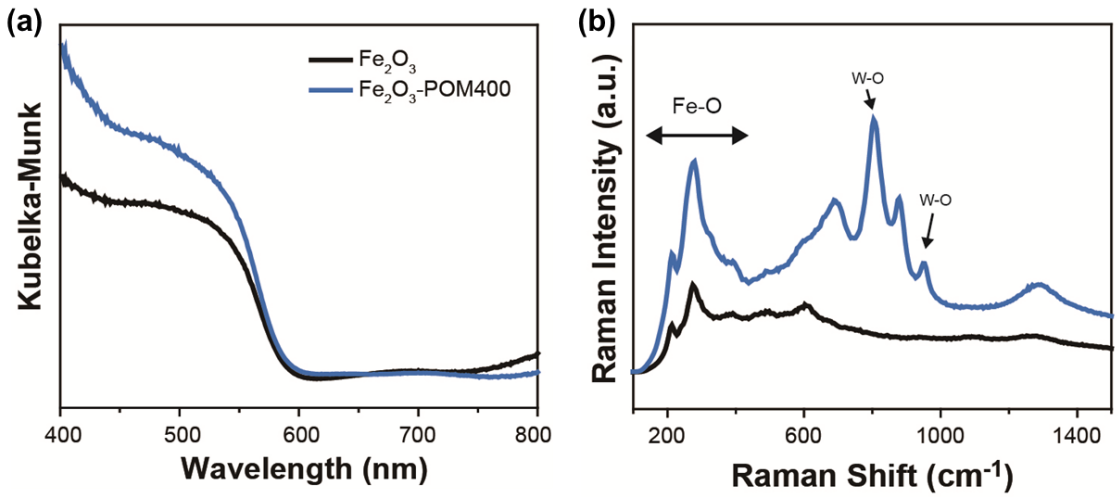

Figure 22. Spectroscopic analysis showing the deposition of POM400 on the surface of hematite photoanodes. (a) Diffuse reflectance and (b) Raman spectra of the photoanodes were compared before and after the deposition of POM400.

3.4.2 Analysis of Photoelectrochemical Catalytic Activity

The deposition of the POM400 significantly improved the performance of the underlying hematite photoanode for visible light-driven water oxidation. As displayed in Figure 23a, the hematite with POM400 cocatalysts exhibited a photocurrent density of 1.36 mA cm^{-2} at 1.23 V *versus* RHE and an onset potential of 0.64 V *versus* RHE that is dramatical increasement compared to the bare hematite and hematite with POM. Polarization curves measured under mild conditions: a low ionic strength (an 80 mM phosphate buffer) and near neutral pH (pH of 8.0) (Table 1) is noteworthy since extreme pH such as 1M NaOH or KOH which is much more advantageous for water oxidation weakens the mechanical strength of photoelectrochemical device. The dark current of hematite with POM400 appearing at 1.45V indicates superior intrinsic activity of POM400 towards water oxidation. In this respect, hematite with POM400 expressed almost three-fold photoelectrochemical activity in chronoamperometry (CA) curves measured at 1.3V *versus* RHE for 3 hours. (Figure 23b) Note that the amount of the deposited POM400 cocatalysts were readily controlled by varying the number of the adsorption processes before annealing also (Figure 23c). A negligible effect on the onset potential for water oxidation was found. However, the photocurrent density increased rapidly with the amount of POM400 cocatalysts up to 10 cycles of the adsorption process and was saturated thereafter.

ULSAN NATIONAL INSTITUTE OF SCIENCE AND TECHNOLOGY

Table 1. Comparison of the photoelectrochemical performance of hematite photoanodes modified with various water oxidation cocatalysts.

Cocatalyst	Onset potential shift (mV)	Onset potential (V)	Electrolyte	Current density (mA cm^{-2})*	Light source	Ref.
POM400	312	0.62	80mM KPi pH 8	1.36	100 mW cm^{-2}	This work
FeNiOOH	190	0.57	1M NaOH	1.11	Xe lamp 100 mW cm^{-2}	43
Ga_2O_3	200	0.8	1M NaOH	0.25 (at 1.02V)	450 W Xe lamp 100mW cm^{-2}	44
Ni-Bi	230	0.62	0.5M KBi	1.12	AM 1.5 100 mW cm^{-2}	45
CoOx	250	0.6	1M KOH	0.65	350 W Xe lamp 100 mW cm^{-2}	46
Co / APA**	290	0.61	1M NaOH	0.97	70W Xe lamp 100 mW cm^{-2}	47
$Co(OH)_2/Co_3O_4$	200	0.9	0.1M KOH	2.1 (at 1.53V)	300W arc lamp AM 1.5	48
IrO_2	200	0.8	1M NaOH	3	AM 1.5 100 mW cm^{-2}	49

* Current density (J) was measured at 1.23V (vs. RHE).
** APA: 3-aminopropionic acid

ULSAN NATIONAL INSTITUTE OF SCIENCE AND TECHNOLOGY

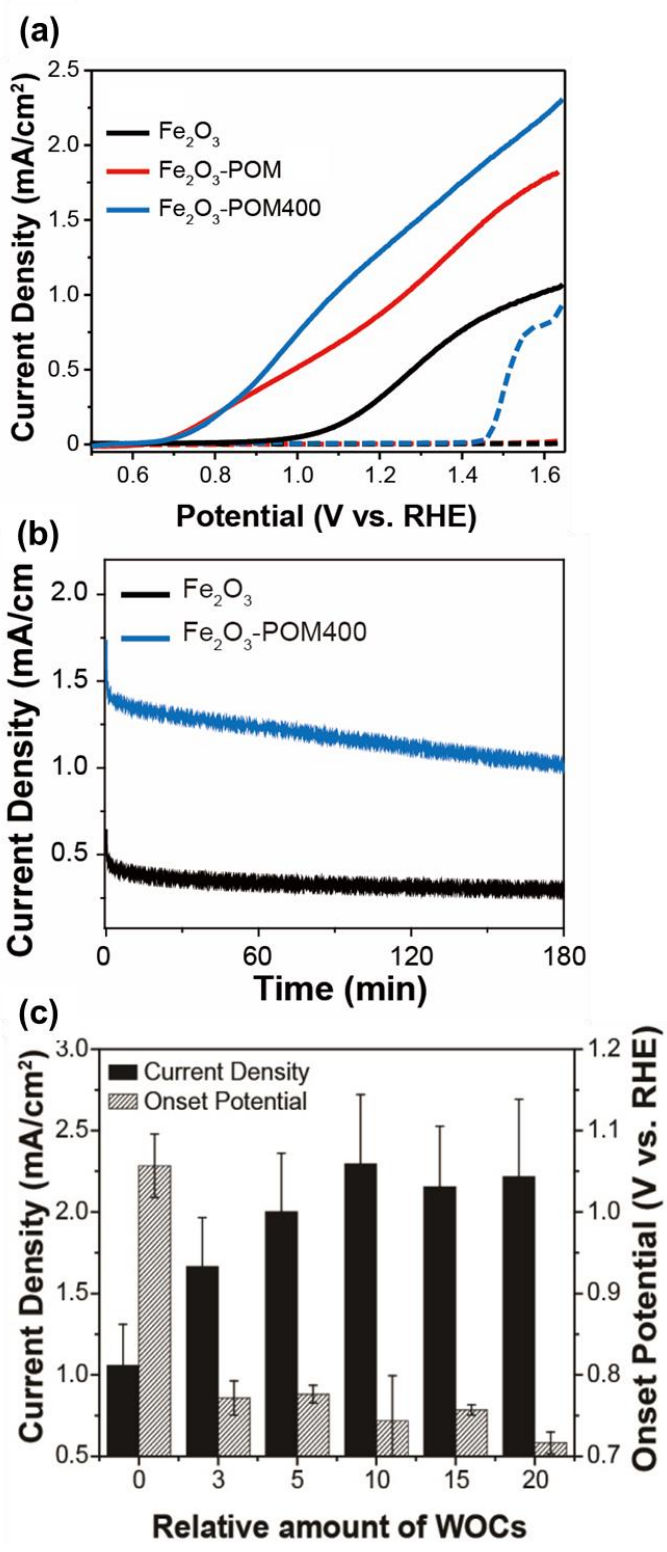

Figure 23. The photoelectrochemical performance of the bare and the modified hematite photoanodes were compared using (a) linear sweep voltammetry, (b) chronoamperometry at 1.3V *versus* RHE and (c) in terms of photocurrent densities and onset potentials.

ULSAN NATIONAL INSTITUTE OF SCIENCE AND TECHNOLOGY

3.5 Additional Analysis for Mechanism Study

Electrochemical impedance spectroscopy (EIS) revealed that the improved photoelectrochemical performance was resulted from the considerable decrease of catalytic charge transfer resistance at the electrode/electrolyte interface (R_2) due to the deposition of the POM400 (Figure 24a and Table 2). Two semicircles in Nyquist plot of hematite with POM400 clearly supported stable deposition of POM on the photoanode. As a result, charge transfer efficiency at the interface was significantly improved. (Figure 24b). Note that the charge transfer efficiency was calculated by comparing photocurrent densities (Figure 25) measured in the presence and absence of a hole scavenger H_2O_2.[41-42] Through the whole potential range from 0.75 V to 1.55 V *versus* RHE, electrode with POM400 presented higher transfer efficiency that bare electrode. As expected, the hematite photoanode with the POM400 produced a much larger amount of oxygen gas than the bare counterpart did (Figure 26). The hydrogen-to-oxygen ratio for the hematite photoanode modified with the POM400 was slightly higher than the theoretical 2:1 ratio but much lower than that for the bare counterpart. The deviation from the theoretical ratio is attributed to the photocorrosion of hematite at around neutral pHs, meaning that the modification of hematite with the POM also improves its stability.

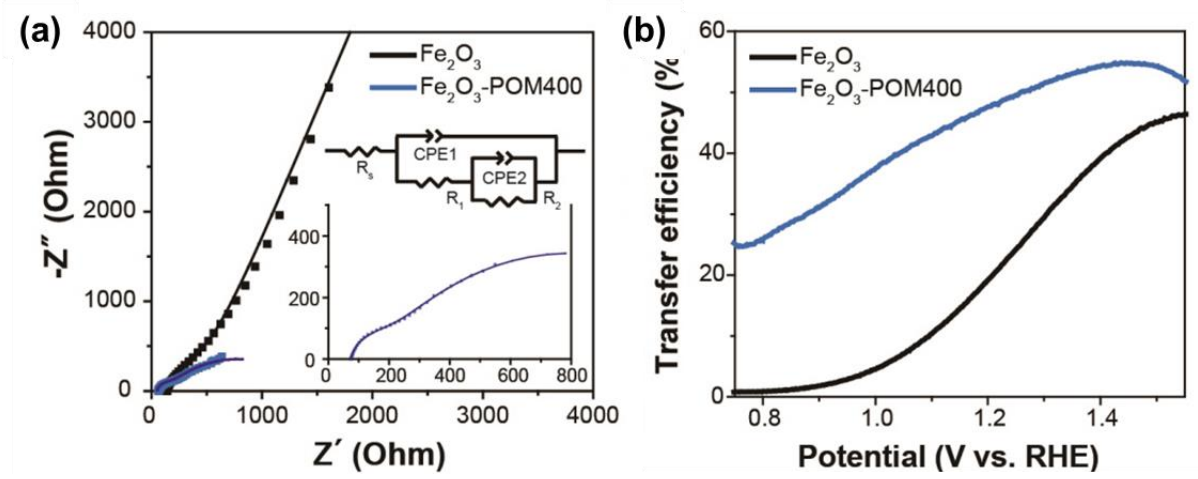

Figure 24. (a) Electrochemical impedance spectra of the bare and modified hematite photoanodes were shown. The inset shows the equivalent circuit model for fitting and the magnified impedance spectra for the modified hematite photoanode. (b) Transfer efficiency plots calculated from J_{photo}-V curves of bare hematite and hematite covered with POM400.

ULSAN NATIONAL INSTITUTE OF SCIENCE AND TECHNOLOGY

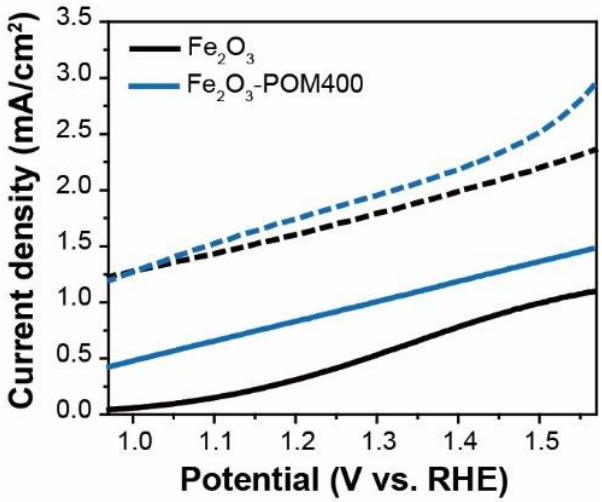

Figure 25. Polarization curves measured in the presence (dotted lines) and absence (solid lines) of 0.1M H_2O_2 for the calculation of the transfer efficiency shown in Figure. 24 (b).

Table 2. Fitting results of the impedance spectra shown in Figure 24a.

	R_S (Ω)	R_1 (Ω)	CPE1 (F)	R_2 (Ω)	CPE2 (F)
Bare	129	938	0.00014	1.128E19	0.00021
POM400	71.23	168	92.3E-6	1178	0.00099

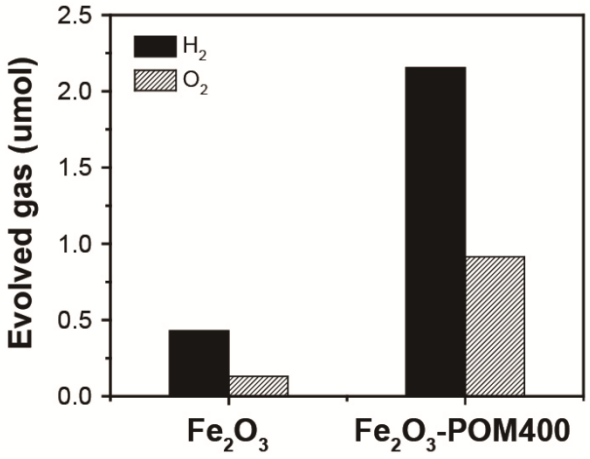

Figure 26. The amount of evolved gases from a PEC cell using a hematite photoanode before and after the modification with POM400 that shows the enhancement of overall PEC performance

ULSAN NATIONAL INSTITUTE OF
SCIENCE AND TECHNOLOGY

Conclusion

In summary, nanoparticulate $CoWO_4$ WOCs were synthesized via the annealing of POMs in air. We found that their structure and catalytic activity for water oxidation highly depend on the annealing temperature. Especially, the POM400 prepared via annealing at 400 °C exhibited an outstanding performance even when compared with the pristine POM, which is a well-known efficient WOC. The annealing of POMs at a higher temperature resulted in a phase transition from a- to c-$CoWO_4$ with a significant decrease of catalytic activity. The superior performance of the POM400 is attributed to its amorphous nature where a high population of Co^{2+}-ion pairs with a shorter nearest-neighbor distance ($D_{Co2+-Co2+}$) exists, facilitating the Langmuir-Hinshelwood (LH) mechanism. Based on these findings, highly efficient electrodes for electrochemical and photoelectrochemical water oxidation were readily prepared through the electrostatic adsorption of POM onto the desired electrode as well as the annealing process. This study not only suggests a new approach to the synthesis of efficient WOCs but also provides insights into the fabrication of various electrochemical systems.

ULSAN NATIONAL INSTITUTE OF SCIENCE AND TECHNOLOGY

References

1. Zou, X.; Zhang, Y., Noble metal-free hydrogen evolution catalysts for water splitting. *Chemical Society Reviews* **2015,** *44* (15), 5148-5180.

2. Chen, Z.; Concepcion, J. J.; Brennaman, M. K.; Kang, P.; Norris, M. R.; Hoertz, P. G.; Meyer, T. J., Splitting CO_2 into CO and O_2 by a single catalyst. *Proceedings of the National Academy of Sciences* **2012,** *109* (39), 15606-15611.

3. Feaster, J. T.; Shi, C.; Cave, E. R.; Hatsukade, T.; Abram, D. N.; Kuhl, K. P.; Hahn, C.; Nørskov, J. K.; Jaramillo, T. F., Understanding Selectivity for the Electrochemical Reduction of Carbon Dioxide to Formic Acid and Carbon Monoxide on Metal Electrodes. *ACS Catalysis* **2017,** *7* (7), 4822-4827.

4. Vesborg, P. C.; Seger, B.; Chorkendorff, I., Recent development in hydrogen evolution reaction catalysts and their practical implementation. *The journal of physical chemistry letters* **2015,** *6* (6), 951-957.

5. Schreier, M.; Curvat, L.; Giordano, F.; Steier, L.; Abate, A.; Zakeeruddin, S. M.; Luo, J.; Mayer, M. T.; Grätzel, M., Efficient Photosynthesis of Carbon Monoxide from CO_2 Using Perovskite Photovoltaics. *Nature communications* **2015,** *6*, 7326.

6. Kang, U.; Choi, S. K.; Ham, D. J.; Ji, S. M.; Choi, W.; Han, D. S.; Abdel-Wahab, A.; Park, H., Photosynthesis of formate from CO_2 and water at 1% energy efficiency via copper iron oxide catalysis. *Energ Environ Sci* **2015,** *8* (9), 2638-2643.

7. Klahr, B.; Gimenez, S.; Fabregat-Santiago, F.; Bisquert, J.; Hamann, T. W., Electrochemical and photoelectrochemical investigation of water oxidation with hematite electrodes. *Energ Environ Sci* **2012,** *5* (6), 7626-7636.

8. Lewis, N. S.; Nocera, D. G., Powering the planet: Chemical challenges in solar energy utilization. *Proceedings of the National Academy of Sciences* **2006,** *103* (43), 15729.

9. Roger, I.; Shipman, M. A.; Symes, M. D., Earth-abundant Catalysts for Electrochemical and Photoelectrochemical Water Splitting. *Nature Reviews Chemistry* **2017,** *1* (1).

10. Fabbri, E.; Habereder, A.; Waltar, K.; Kotz, R.; Schmidt, T. J., Developments and Perspectives of Oxide-based Catalysts for The Oxygen Evolution Reaction. *Catalysis Science & Technology* **2014,** *4* (11), 3800-3821.

11. Blakemore, J. D.; Crabtree, R. H.; Brudvig, G. W., Molecular Catalysts for Water Oxidation. *Chem Rev* **2015,** *115* (23), 12974-3005.

12. Tachibana, Y.; Vayssieres, L.; Durrant, J. R., Artificial Photosynthesis for Solar Water-splitting. *Nature Photonics* **2012,** *6*, 511.

13. Sinclair, T. S.; Hunter, B. M.; Winkler, J. R.; Gray, H. B.; Muller, A. M., Factors Affecting

ULSAN NATIONAL INSTITUTE OF SCIENCE AND TECHNOLOGY

Bismuth Vanadate Photoelectrochemical Performance. *Materials Horizons* **2015,** *2* (3), 330-337.

14. McKone, J. R.; Lewis, N. S.; Gray, H. B., Will Solar-Driven Water-Splitting Devices See the Light of Day? *Chemistry of Materials* **2014,** *26* (1), 407-414.

15. Bhatt, M. D.; Lee, J. S., Recent Theoretical Progress in The Development of Photoanode Materials for Solar Water Splitting Photoelectrochemical Cells. *Journal of Materials Chemistry A* **2015,** *3* (20), 10632-10659.

16. Brimblecombe, R.; Dismukes, G. C.; Swiegers, G. F.; Spiccia, L., Molecular Water-oxidation Catalysts for Photoelectrochemical Cells. *Dalton Transactions* **2009,** (43), 9374-9384.

17. Zhang, M.; de Respinis, M.; Frei, H., Time-resolved Observations of Water Oxidation Intermediates on a Cobalt Oxide Nanoparticle Catalyst. *Nat Chem* **2014,** *6* (4), 362-7.

18. Duan, L.; Wang, L.; Li, F.; Li, F.; Sun, L., Highly Efficient Bioinspired Molecular Ru Water Oxidation Catalysts with Negatively Charged Backbone Ligands. *Accounts of Chemical Research* **2015,** *48* (7), 2084-2096.

19. Moore, G. F.; Blakemore, J. D.; Milot, R. L.; Hull, J. F.; Song, H.-e.; Cai, L.; Schmuttenmaer, C. A.; Crabtree, R. H.; Brudvig, G. W., A Visible Light Water-splitting Cell with a Photoanode Formed by Codeposition of a High-potential Porphyrin and an Iridium Water-oxidation Catalyst. *Energy & Environmental Science* **2011,** *4* (7), 2389-2392.

20. Luo, J.; Im, J.-H.; Mayer, M. T.; Schreier, M.; Nazeeruddin, M. K.; Park, N.-G.; Tilley, S. D.; Fan, H. J.; Grätzel, M., Water Photolysis at 12.3% Efficiency via Perovskite Photovoltaics and Earth-abundant Catalysts. *Science* **2014,** *345* (6204), 1593-1596.

21. Diaz-Morales, O.; Raaijman, S.; Kortlever, R.; Kooyman, P. J.; Wezendonk, T.; Gascon, J.; Fu, W.; Koper, M. T., Iridium-based Double Perovskites for Efficient Water Oxidation in Acid Media. *Nature communications* **2016,** *7*, 12363.

22. Lee, J. G.; Hwang, J.; Hwang, H. J.; Jeon, O. S.; Jang, J.; Kwon, O.; Lee, Y.; Han, B.; Shul, Y.-G., A New Family of Perovskite Catalysts for Oxygen-evolution Reaction in Alkaline media: $BaNiO_3$ and $BaNi_{0.83}O_{2.5}$. *Journal of the American Chemical Society* **2016,** *138* (10), 3541-3547.

23. Yu, X.; Zhang, M.; Yuan, W.; Shi, G., A high-performance Three-dimensional Ni-Fe Layered Double Hydroxide/graphene Electrode for Water Oxidation. *Journal of Materials Chemistry A* **2015,** *3* (13), 6921-6928.

24. Kärkäs, M. D.; Åkermark, B., Water Oxidation Using Earth-abundant Transition Metal Catalysts: Opportunities and Challenges. *Dalton Transactions* **2016,** *45* (37), 14421-14461.

25. Kanan, M. W.; Nocera, D. G., In situ Formation of an Oxygen-evolving Catalyst in Neutral Water Containing Phosphate and Co2+. *Science* **2008,** *321* (5892), 1072-1075.

26. Zhou, Y.; Chen, G. J.; Long, Z. Y.; Wang, J., Recent Advances in Polyoxometalate-based Heterogeneous Catalytic Materials for Liquid-phase Organic Transformations. *Rsc Adv* **2014,** *4* (79),

ULSAN NATIONAL INSTITUTE OF SCIENCE AND TECHNOLOGY

42092-42113.

27. Bi, L.-H.; Kortz, U.; Nellutla, S.; Stowe, A. C.; van Tol, J.; Dalal, N. S.; Keita, B.; Nadjo, L., Structure, Electrochemistry, and Magnetism of the Iron(III)-Substituted Keggin Dimer, $[Fe_6(OH)_3(A\text{-}\alpha\text{-}GeW_9O_{34}(OH)_3)_2]^{11-}$. *Inorganic Chemistry* **2005,** *44* (4), 896-903.

28. Weinstock, I. A., Homogeneous-Phase Electron-Transfer Reactions of Polyoxometalates. *Chemical Reviews* **1998,** *98* (1), 113-170.

29. Sartorel, A.; Carraro, M.; Scorrano, G.; Zorzi, R. D.; Geremia, S.; McDaniel, N. D.; Bernhard, S.; Bonchio, M., Polyoxometalate Embedding of a Tetraruthenium(IV)-oxo-core by Template-Directed Metalation of $[\gamma\text{-}SiW_{10}O_{36}]^{8-}$: A Totally Inorganic Oxygen-Evolving Catalyst. *Journal of the American Chemical Society* **2008,** *130* (15), 5006-5007.

30. Yin, Q. S.; Tan, J. M.; Besson, C.; Geletii, Y. V.; Musaev, D. G.; Kuznetsov, A. E.; Luo, Z.; Hardcastle, K. I.; Hill, C. L., A Fast Soluble Carbon-Free Molecular Water Oxidation Catalyst Based on Abundant Metals. *Science* **2010,** *328* (5976), 342-345.

31. Huang, Z.; Luo, Z.; Geletii, Y. V.; Vickers, J. W.; Yin, Q.; Wu, D.; Hou, Y.; Ding, Y.; Song, J.; Musaev, D. G.; Hill, C. L.; Lian, T., Efficient Light-driven Carbon-free Cobalt-based Molecular Catalyst for Water Oxidation. *J Am Chem Soc* **2011,** *133* (7), 2068-71.

32. Jeon, D.; Kim, H.; Lee, C.; Han, Y.; Gu, M.; Kim, B.-S.; Ryu, J., Layer-by-Layer Assembly of Polyoxometalates for Photoelectrochemical (PEC) Water Splitting: Toward Modular PEC Devices. *ACS applied materials & interfaces* **2017,** *9* (46), 40151-40161.

33. Lauinger, S. M.; Piercy, B. D.; Li, W.; Yin, Q.; Collins-Wildman, D. L.; Glass, E. N.; Losego, M. D.; Wang, D.; Geletii, Y. V.; Hill, C. L., Stabilization of Polyoxometalate Water Oxidation Catalysts on Hematite by Atomic Layer Deposition. *ACS applied materials & interfaces* **2017,** *9* (40), 35048-35056.

34. Chen, W.; Huang, L.; Hu, J.; Li, T.; Jia, F.; Song, Y. F., Connecting Carbon Nanotubes to Polyoxometalate Clusters for Engineering High-performance Anode Materials. *Physical Chemistry Chemical Physics* **2014,** *16* (36), 19668-19673.

35. Gupta, S.; Aberg, B.; Carrizosa, S. B., Functionalized Graphene–Polyoxometalate Nanodots Assembly as "Organic–Inorganic" Hybrid Supercapacitors and Insights into Electrode/Electrolyte Interfacial Processes. *C* **2017,** *3* (3), 24.

36. Zhang, W.; Li, W.; He, X.; Zhao, L.; Chen, H.; Zhang, L.; Tian, P.; Xin, Z.; Fang, W.; Zhang, F., Dendritic Fe-based Polyoxometalates@ metal–organic framework (MOFs) Combined with ZnO as a Novel Photoanode in Solar Cells. *Journal of Materials Science: Materials in Electronics* **2018,** *29* (2), 1623-1629.

37. Dotan, H.; Sivula, K.; Grätzel, M.; Rothschild, A.; Warren, S. C., Probing the Photoelectrochemical Properties of Hematite ($\alpha\text{-}Fe_2O_3$) Electrodes Using Hydrogen Peroxide as a Hole

ULSAN NATIONAL INSTITUTE OF SCIENCE AND TECHNOLOGY

Scavenger. *Energ Environ Sci* **2011,** *4* (3), 958-964.

38. Gao, Y.; Hamann, T. W., Quantitative Hole Collection for Photoelectrochemical Water Oxidation with $CuWO_4$. *Chemical Communications* **2017,** *53* (7), 1285-1288.

39. Gil, A. L.; Milliron, D. J.; LeBlanc, G.; Wang, Y. Methods for Producing Electrochromic Films by Low Temperature Condensation of Polyoxometalates. 2017.

40. Ensafi, A. A.; Heydari-Soureshjani, E.; Jafari-Asl, M.; Rezaei, B., Polyoxometalate-decorated Graphene Nanosheets and Carbon Nanotubes, Powerful Electrocatalysts for Hydrogen Evolution Reaction. *Carbon* **2016,** *99*, 398-406.

41. Jia, H.; Stark, J.; Zhou, L. Q.; Ling, C.; Sekito, T.; Markin, Z., Different Catalytic Behavior of Amorphous and Crystalline Cobalt Tungstate for Electrochemical Water Oxidation. *RSC Advances* **2012,** *2* (29), 10874-10881.

42. Zhong, D. K.; Cornuz, M.; Sivula, K.; Grätzel, M.; Gamelin, D. R., Photo-assisted Electrodeposition of Cobalt–phosphate (Co–Pi) Catalyst on Hematite Photoanodes for Solar Water Oxidation. *Energ Environ Sci* **2011,** *4* (5), 1759-1764.

ULSAN NATIONAL INSTITUTE OF
SCIENCE AND TECHNOLOGY

Acknowledgement

어느새, UNIST에서 학생으로 보냈던 시간들이 끝나가고 졸업을 앞두고 있습니다. 그 동안 있었던 크고 작은 일들 사이에서 항상 저를 격려해주고 응원해주었던 많은 분들께 모두 감사인사 드립니다. 앞으로 또 수많은 일들이 펼쳐지겠지만 이 곳에서의 소중했던 경험들을 잊지 못할 것 같습니다.

특히나, 제가 다양한 경험을 할 수 있도록 이끌어 주신 류정기 교수님께 정말 감사드립니다. 아낌없는 조언과 격려로 항상 최선을 다해 지도해 주신 교수님이 계셨기에 많은 것을 배울 수 있었습니다. 또한 학위 심사를 맡아 조언 해주신 송현곤 교수님과 이현욱 교수님께도 감사드립니다. 교수님들의 말씀을 바탕으로 더욱 노력하겠습니다.

마지막으로 제 주변에서 또는 멀리서 항상 애정 어린 격려와 응원의 말을 해준 가족들과 친구들 모두 감사드립니다. 앞으로 더욱 멋있고 열정적인 사람이 되도록 끊임없이 노력하겠습니다. 모두 감사합니다.

ULSAN NATIONAL INSTITUTE OF
SCIENCE AND TECHNOLOGY